Photon Sources

for Lithography and Metrology

Vivek Bakshi, *Editor*

SPIE PRESS
Bellingham, Washington USA

Library of Congress Cataloging-in-Publication Data

Names: Bakshi, Vivek, editor.
Title: Photon sources for lithography and metrology / Vivek Bakshi, editor.
Identifiers: LCCN 2022055893 | ISBN 9781510653719 (hardcover) | ISBN 9781510653726 (pdf)
Subjects: LCSH: Extreme ultraviolet lithography. | Laser plasmas. | Speckle metrology. | Holography. | Ultraviolet radiation–Industrial applications. | Lasers–Industrial applications.
Classification: LCC TK7872.M3 P473 2023 | DDC 621.3815/31–dc23/eng/20230113
LC record available at https://lccn.loc.gov/2021039247

Published by
SPIE
P.O. Box 10
Bellingham, Washington 98227-0010 USA
Phone: +1 360.676.3290
Fax: +1 360.647.1445
Email: books@spie.org
Web: https://spie.org

Images in lower portion of front cover are photographs of Energetiq Technology's Laser-Driven Light Source (LDLS™) bulb and Electrodeless Z-Pinch™ EUV plasma, used with permission.

Printed in the United States of America.
First printing 2023.
For updates to this book, visit https://spie.org and type "PM351" in the search field.

SPIE.

This book is dedicated to the scientists and engineers who have believed in the potential of EUVL, to those who have invested in EUVL to ensure its status as a technology used in fabs and HVM, enabling the continued extension of Moore's law, and to all those who have contributed to the success of EUVL.

Contents

Foreword

The challenges posed by Moore's law have driven research and innovation in the semiconductor industry for the past six decades. Since the early 1960s, the need to print smaller and smaller features using projection lithography systems and the need to overcome diffraction limitations has resulted in the source wavelength decreasing from 436 nm, which can produce features with sizes of tens of microns, to 13.5 nm, which can produce feature sizes of 7-nm nodes in the latest tools being produced today by ASML. Along the way, sources changed from Hg discharge lamps [operating at wavelengths of 436 nm (g-line), 405 nm (h-line), and 365 nm (i-line) in the near-ultraviolet (UV)] to excimer lasers, operating first at 248 nm and later at 193 nm, to laser-produced plasmas that emit in the extreme ultraviolet (EUV) at 13.5 nm. While the move from discharge lamps to lasers involved a relatively small and gradual reduction in wavelength over time, the step change to 13.5-nm operation, predicated on the availability of Si-Mo multilayer mirrors, involved a radical change in source technology as both reflective optics and high-vacuum operation were now required.

The drive to develop a suitable source soon became the main obstacle to be overcome for the successful implementation of EUV lithography in high-volume manufacturing fabs. The first real demonstration of the feasibility of EUV lithography using 13.5-nm optics was made by the Engineering Test Stand at Sandia National Laboratories in 2001–2002 using a laser-produced plasma from a Xe cluster source. It was long known that the integrated EUV intensity from high-Z plasmas generally exceeds that from lower-Z plasmas, and Xe has the advantage that a group of resonance lines from Xe^{10+} emits in the 13.5 nm region. However, although it was known that Sn provides a potentially more intense source, there was initially reluctance to use Sn plasmas because Xe, being a gaseous fuel, was less challenging to deal with, especially in a discharge plasma, and was also more attractive from a debris mitigation viewpoint. During the preceding 30 years, one of the most researched areas in EUV spectroscopy had been the photoionization of 4d electrons in the elements around Xe whose spectra were completely dominated by intense shape resonances. Theoretical and experimental studies clearly showed that with increasing ionization, the oscillator strength associated with these resonances was gradually transferred to 4d–4f transitions. Thus, the latter could be expected

to completely dominate spectra of highly charged ions of these species with open 4d subshells. However, because these transitions tend to overlap in adjacent ion stages and owing to their very large transition probabilities, radiation transport is a major issue. Indeed, early work on ruby and Nd:YAG laser-produced plasmas at University College Dublin (UCD) demonstrated that the emission from targets containing a small percentage of the relevant element was actually more intense than the emission from pure targets. Because of the complexity of the transitions involved, the emission consisted of a broad quasi-continuum feature overlaid by many strong lines and was labeled an unresolved transition array (UTA) by Jacques Bauche, Claire Bauche-Arnoult, and Marcel Klapisch in *Physica Scripta* in 1983. It had been demonstrated that the UTA emission in Sn peaked near the required wavelength of 13.5 nm.

Although the potential advantages of using Sn were clear and were being pushed by a number of researchers, including Toshihisa Tomie at the National Institute of Advanced Industrial Science and Technology, Tsukuba, Martin Richardson at the University of Central Florida, and the Spectroscopy Group at UCD, it was not until industry set a power requirement in excess of 200 W in intermediate focus that research on Sn sources began in earnest. Initially, studies on laser-produced plasmas were largely confined to university groups such as those at ILE Osaka, Utsunomiya University, and University of California San Diego, while considerable progress using discharge-produced plasma (DPP) or hybrid laser-driven discharge-produced plasma (called LDP) sources was reported by industry represented by, among others, Cymer and AIXUV (for DPP) and Philips and Xtreme Technologies, and later Ushio (for LDP). However, by around 2006, it was clear that the power requirement could not be met by discharge plasmas, and the modeling effort being driven especially by the groups led by Katsunobu Nishihara at ILE Osaka and the late Vladimir Novikov at the Keldysh Institute paved the way in terms of dual-pulse-irradiated Sn-droplet sources. To reduce the plasma density and the problems posed by plasma opacity, the main pulse used was produced by a high-repetition-rate CO_2 laser. Pioneering work on CO_2 laser development and dual-pulse illumination then commenced at Gigaphoton, who clarified the viability of laser-produced plasma sources for high-volume manufacturing.

Since then, a major experimental and modeling effort has greatly increased our understanding of the physics of Sn sources and has pointed to ways in which their in-band emission may be optimized. Noteworthy early work was performed by groups at Troitsk, the University of California San Diego, Purdue University, EPPRA, Tokyo Metropolitan University, and the National Institute for Fusion Science, Toki, Japan. In particular, the work at the Advanced Research Center for Nanolithography (ARCNL) Source Group (presented in Chapter 4) has shown the importance of transitions between multiply excited states, first considered by Akira Sasaki of the Kansai Photon Science Institute to explain the broadening of the Sn UTA. As discussed in Chapters 3 and 5, recent modeling has shown that

there is still room for improvement in terms of the conversion of laser power to useful EUV radiation and points toward the possibility of using mid-IR lasers in future sources. In subsequent chapters, the industrial realization of current sources by Cymer/ASML and Gigaphoton is discussed, as well as a variety of discharge, laser-driven-discharge, and laser-produced-plasma sources that can be used for metrology and EUV irradiation studies. Although not useful for high-volume production, discharge sources are still invaluable for other very relevant applications such as metrology, testing, and R&D, many of which are the topic of later chapters. Other topics covered are improvements in EUV optical design and debris mitigation as well as new solid state laser concepts and potential future roles for sources based on high harmonic generation and electron accelerators. To produce smaller features, the possibility of using Gd plasmas emitting at 6.7 nm has been suggested by the late Sergei Churilov and his co-workers in Troitsk and explored extensively by Takeshi Higashiguchi and his group at Utsunomiya University. Producing the increased in-band power required for future lithography sources remains a challenge to be overcome and may indeed require another disruptive shift, this time to free-electron lasers and the use of diffractive optics that will exploit the coherence properties of such sources.

In addition to EUV sources, this book also covers synchrotrons (Chapters 17 and 24), free-electron lasers or FELs (Chapter 25), and high harmonic generation or HHG (Chapter 21), which have and continue to support EUVL development. For the sake of completeness, Chapter 20 also covers additional lasers at 193 nm (ArF lasers), 248 nm (KrF lasers), and 157 nm (F_2 lasers), Chapter 26 covers UV lamps, which provide the photons at i-line (365 nm), h-line (405 nm) and g-line (436 nm) wavelengths. These lasers and UV lamps have driven the development of successive generations of lithography tools and continue to be widely used by the industry.

This book is essential reading for anyone working on EUV sources for lithography, metrology, or EUV irradiation studies or anyone interested in the physics and engineering challenges that had to be overcome to realize the current generation of EUV lithography tools, written by the people from industry and academia who made it happen. It also looks to future developments and obstacles that must be overcome to enable the technology to persist into the future. Thanks to the hard work of many people, the vision of researchers like the late Akiro Endo, and the annual EUV Lithography and EUV Lithography Source workshops organized by Vivek Bakshi of EUV Litho, Inc., which provide an invaluable bridge between industry and academia, a lot has been achieved. However, for researchers working in this challenging and exciting field, still more remains to be done, and the next decade should witness many novel and interesting developments.

Gerry O'Sullivan
University College Dublin, Ireland

Preface

It brings me joy to get *Photon Sources for Lithography and Metrology* into the hands of my readers. As the key drivers of the extension of Moore's law, photon sources enable the extension of lithography and metrology technologies for continued scaling of circuit elements. In this Preface, I want to give you some context for the subject matter of this volume, as well as the reason I produced it to begin with: to serve the community of consumers and researchers in the advanced semiconductor chip manufacturing industry.

At the time of this book's publication, extreme ultraviolet lithography (EUVL) is in high-volume production (HVM) and has continued the extension of Moore's law by enabling dimensional scaling of features. It is also believed that the current 0.33 NA EUVL scanner, together with its high-NA version of 0.55, will continue to extend Moore's law for at least a decade or two. It has taken almost 35 years to get the technology ready for HVM. In the early 2000s, when serious efforts to commercialize EUVL were taking place, EUV sources were considered the biggest obstacle to the success of EUV lithography. However, the persistence of EUV source researchers ensured that EUVL would become a reality.

In early 2000, while managing EUV source projects at SEMATCH, I compiled the latest knowledge on this topic for the benefit of researchers and suppliers in the industry. This resulted in my previous book on the topic of photon sources, *EUV Sources for Lithography* (SPIE Press, 2006), which was met with acclaim from the community. At that time, EUVL was "soon to be adopted in fabs for high-volume manufacturing" as soon as EUV sources were able to meet the requirements of $\sim$100 W. Efforts were being made on various fronts: modeling, fundamental data, new materials, and prototype development.

At that time, the EUVL industry also needed to decide between laser-produced plasmas (LPPs) and discharge-produced plasmas (DPPs), both of which could be utilized to meet power-scaling requirements for EUVL scanners. LPP had the advantage of various drive lasers, ranging from excimer to CO_2. At the same time, DPP also had various competing designs. The choice of fuel for EUV sources was also a hot topic of debate, with options ranging from xenon to tin and even lithium. The list of challenges surrounding EUV sources grew longer, with conflicting opinions on materials, laser drivers, collectors, out-of-band filters, and debris mitigation only adding

to the list. One leading expert and my mentor even feared that debris mitigation would be the fatal flaw behind EUVL, increasing alongside the output of power. While considering the material for the edited volume, I wanted to cover the topic from every angle possible. As a result, *EUV Sources for Lithography* grew to be 38 chapters long!

As time passed, and as source technology underwent rapid development, I was requested to provide an updated version of the EUV source book. However, I decided on a different approach to produce a book on EUV lithography as a whole. I wanted to include all components of the topic: sources, optics, resist, system design contamination, imaging, cost of ownership, etc. *EUV Lithography* was released in 2009 by SPIE Press. Meanwhile, steady progress was being made towards EUV source technology and EUVL scanners. The competition between suppliers shrank considerably, and the industry anticipated the implementation of HVM in the near future—a hope that would later be revealed to take much longer than expected. EUV source choices for EUVL scanners were narrowed to Sn LPP, although there was still the issue of power requirements for these sources. Demand for an updated book for on EUVL and EUV source topics increased. In response, I directed readers to the extensive, excellent database of EUVL papers from SPIE, as well as the open access presentations from annual EUVL and EUV Source Workshops that I had been organizing since 2008. These presentations continue to be available on www.euvlitho.com.

The early 2010s were very difficult years for EUVL development. Skepticism among traditional lithography experts expanded across the industry, and their criticisms did not go unheard. The limited progress towards EUV source power certainly did not help to appease the skeptics. Chip makers were ready to adopt EUVL as soon as it became available, as multi-patterning immersion lithography with 193 nm had difficulties sustaining Moore's law. However, EUVL technology was not yet ready for HVM, mainly due to the absence of EUV sources for EUVL scanners. But I maintained hope; these engineering challenges were merely hurdles to overcome in the name of progress. While being a public advocate for this technology, I continued to work and promote EUVL via publications, workshops, and education, all which I continue to do today.

During that time, I decided that, instead of updating the source or lithography book, a collection of selected papers from the SPIE database would serve the readers instead. Together with Anthony Yen, I published a volume with selected papers from *Proc. SPIE* and the SPIE journal *JM3* in 2012, entitled *Extreme Ultraviolet Lithography*. I realized that this was merely an improvised solution, and my readers were in dire need of the latest EUV technical information. So, I spent another three years producing the second edition of *EUV Lithography* with SPIE Press in 2018. This book would go on to become an instant bestseller!

In 2018, Samsung became the first company to announce the use of EUVL for product manufacturing. Since then, companies such as TSMC and Intel as well as several others are either already using or have included EUV within their production plans for HVM. Several other manufacturers, like Hynix and Micron, have recently announced their plans to adopt the use EUVL in HVM within the coming year. Because EUVL is now adopted at 0.33 NA, I am positive that this list will continue to expand.

Circling back to the topic of EUV sources, there's been success involving EUV sources with regards to providing the necessary sources for the insertion of EUVL in HVM. Today, EUV sources are no longer the leading challenge for EUVL. Now the focus is on EUV resists and infrastructure development. By 2018, the dilemma of EUV source technology choices was resolved, but new challenges arose, thanks to the ever-increasing demand for new technology to sustain Moore's law. Focus has now shifted from viability to the extension of technology to the next node, increasing reliability (by reducing downtime), and reducing the cost of ownership. We are also now looking at the potential of wavelength reduction to "Blue-X," which may be 6.7 nm or less for the next generation of scanners and metrology tools. The material in the 2018 volume, *EUV Lithography, Second Edition*, is based on current technologies that are either already being used in fab or are slated to be used in the near future. The topics presented in that book are also of relevance to extension of sources for EUVL via wavelength reduction or Blue-X.

Today, ASML is the only supplier of EUVL scanners. Cymer, the leading supplier of EUV sources, was acquired by ASML, and, currently, all EUV sources in scanners are made by Cymer. The second supplier of EUV sources for scanners, Gigaphoton, continues its efforts in EUV source development and is now looking for metrology applications for its EUV sources as well. The landscape of EUV metrology sources is still not settled, as these sources continue to be developed to support the continuously evolving requirements for metrology tools. The actinic inspection of mask defects at 13.5 nm has been shown to be superior to inspections done by 193-nm lasers and are needed for future nodes. However, as this book will later explain, metrology EUV sources, as compared to those needed for scanners, need to be smaller in size and need less power but must be brighter.

Until recently, Xe DPP sources have been the main drivers of metrology tools for mask inspection, optics and system testing, resist testing, and many other areas. However, more power and higher brightness is needed, especially for actinic patterned mask defect inspection (APMI) tools. Laser-driven DPP sources from USHIO, which are also covered in this volume, have been adopted by one supplier for APMI for their prototype tools, while other LPP sources are being evaluated. In short, EUV sources for metrology is still an active area of commercial development. Several other suppliers are working on DPP, LPP, and other technologies such as high harmonic generation to

continue developing sources for the use of additional applications in metrology and R&D to support EUVL.

To further extend Moore's law and improve resolution, ASML, the only current supplier of EUVL scanners, has increased the NA from 0.33 to 0.55, for their next generation of EUVL scanners, called high-NA EUVL scanners. With time, these high-NA scanners will also be used for multi-patterning to enable continued extension of Moore's law, as was done for 193-nm immersion lithography. Use of scanners with lower k_1 values, innovative resists, higher NA, and multi-pattering will all require additional power. The task of producing debris-free EUV photons will be an on-going challenge for this decade and beyond. Success on this front will require thorough analysis of fundamental dynamics via experiments, with the support of modeling and updated fundamental data. These efforts continue today and are documented in this volume.

In addition to plasma sources, we must note that lasers have continued to be a vital focus of research, as they are the driver for LPP. Their development will enable higher-power EUVL sources or potential extension of EUV sources to a shorter wavelength. Industry experts looked into 6.7-nm lithography a decade ago, but then gave up in order to focus on 13.5-nm lithography. At that time, these efforts were known as beyond EUV (BEUV). However, I came to the realization that beyond high-NA multi-patterning (high-NA MP), the industry had limited choices. So, in 2018, I decided to restart the effort of extension of EUVL by wavelength reduction and gave it a new name: Blue-X.

I revitalized this project with the purpose of reviewing several options of reduced wavelength from 13.5 to the water window. I also realized that, in order to enable these Blue-X photon sources to support EUVL extension, we will need higher-powered lasers—power that 10-μm CO_2 lasers cannot provide. Our attention should turn to solid state lasers, such as 2-μm thulium lasers. This development will require serious efforts supported by modeling and fundamental research. I believe that these efforts will also benefit the current 13.5-nm-based sources, which will continue to increase in power and conversion efficiency and reduce debris. While discussing power extension for EUVL—which is predicted to reach 1 kW or more —we need to also discuss free-electron lasers (FELs). FELs were originally thought to be a potential choice of high-power sources for EUVL. Some industry groups continue to believe in the potential of FELs and continue to work towards their development for EUVL. As such, we have included FEL sources in this volume.

The topic of high harmonic generation (HHG) is also included in this volume. Today, HHG-based EUV sources continue to be used in mask inspection metrology tools as well as in imaging. For the past several years, due to the absence of HVM-level APMI tools, HHG has been primarily used by chip makers. But I believe that HHG-based metrology will continue to find a role in supporting EUVL R&D.

Based on these points, this volume contains material on modeling, lasers, and fundamental data, and coverage of DPP, LDP, and FEL. For sources, I have restricted the coverage to EUV sources and topics pertaining to the future of 13.5-nm Sn LPP as well as a possible Blue-X extension. We have also added excimer lasers, as 193-nm-based lithography was the most advanced lithography until the recent implementation of EUVL. 193-nm lithography will continue to be in use for the foreseeable future. For much larger features in the back end of circuits, the industry still uses DUV lamps—a photon source that will also continue to have use in the future. Despite the widespread usage of these sources, there has not been a written text to explain their status and the challenges behind them. So, for the benefit of the community, we have included them in this book.

With the timeline leading to this current volume in place, I will now proceed to give readers a brief overview of the content covered in this book.

Part I (Chapter 1) gives an overview of the technology, status, and requirements of current EUV sources employed in EUV scanners, metrology, and R&D applications. Chapter 1 is a brief, high-level summary of covered topics; in it, the reader is referred to other chapters for additional information. This chapter serves as an introduction to the subject matter, including the basics, current requirements, and future challenges the technology may face. This chapter also briefly covers EUV source technologies that could potentially be used for the extension of EUVL, which may be needed for higher-power or shorter-wavelength (Blue-X) sources.

Part II (Chapters 2–5) covers fundamentals and modeling for EUV sources. Chapter 2 provides insight into the atomic physics of unresolved transition arrays (UTAs) of tin, which provide 13.5-nm photons for EUVL. It also covers other elements that will be candidates for source material at wavelengths shorter than 13.5 nm and up to water window wavelengths. These short-wavelength sources could enable further reduction of wavelengths for the extension of optical projection lithography. In addition to lithography, short-wavelength sources are being used for imaging in the water windows for medical applications. Chapters 3 and 5 cover plasma modeling, which is an important component in designing and improving Sn LPP sources. Chapter 3 discusses the radiation-hydrodynamics (RH) models, which are used to understand the physics of Sn LPP sources and to guide the development of these sources. In Chapter 5, the authors describe the physical aspects and challenges for numerical modeling of plasma, with examples from their RALEF code. Chapter 4 provides details on atomic transitions for tin that are responsible for emissions in the EUV region. It also discusses the application of opacity tables for local thermodynamic equilibrium (LTE) plasma for modeling non-LTE plasmas to simplify calculations.

Part III (Chapters 6–12) covers the sources that are currently being used in HVM fabs. Chapter 6 covers Sn LPP from Cymer (now part of ASML) and is

a reprint from *EUV Lithography, 2nd edition* because not much in regard to the fundamentals of these sources has changed, although, impressive power scaling to ~500 W and significant lifetime improvement have been achieved. This source is the major contributor to the successful implementation of EUVL in fabs today!

Chapter 7 from Gigaphoton covers their technology on Sn LPP sources, which are also driven by a CO_2 laser. Although most of the technology is similar to that described in Chapter 6, there are key differences in terms of magnetic debris mitigation and the use of 1-μm Nd:YAG laser for pre-pulses.

The next five chapters cover photon sources being used for metrology in EUVL and metrology for general semiconductor manufacturing purposes. Chapter 8 from Energetiq describes their DPP source, which is an inductively coupled xenon Z-pinch source. Inductive coupling and a unique design enable a stable and long-term operation of their source, which has allowed the early adoption of this source by the industry in metrology tools and for general R&D. However, for actinic inspection of mask defects, higher brightness and power is needed, which may require the use of additional sources. Chapter 9 covers laser-assisted DPP sources from Ushio, which have now been adopted in a first prototype of APMI metrology tools. This technology, while initially used in alpha- and beta-level EUV scanners, now finds use in metrology, following the industry's move to Sn LPP for scanners. This source is a tin DPP source, where electrodes are embedded in a tin bath to cure erosion and tin is supplied for discharge via a laser focused on the tin electrodes.

Chapter 10 outlines R&D and initial development work at Fraunhofer for hollow-cathode-triggered Xe DPP sources. Their design has been successful in providing additional short-wavelength sources by changing the fuel. The authors are now using their Xe DPP source for powering R&D exposure tools. The concept was commercialized as a low-power version for metrology applications in the early 2000s by AIXUV, a Fraunhofer spin-off. This source is covered in Chapter 11. It is now available from Research Instruments and is being used in their various metrology tools to support EUVL.

Chapter 12 diverges from the topic of EUV sources and covers a laser-driven plasma source that produces photons in the UV–Vis–IR region (200–900 nm). This technology has found successful applications in the semiconductor industry.

Part IV (Chapters 13–18) covers the topics of optics and metrology related to EUV and short-wavelength sources. Metrology has played a key part in the development of EUVL. In early 2000, after the first set of EUV sources gained the potential to power scanners, the first step was to make a reliable absolute measurement of in-band power. The Flying Circus (FC) program (which I managed from SEMATECH at the time) was tasked with ensuring that we were aware of the reliable status of source performance. FC was constructed by a group at the FOM in the Netherlands; this group is now part of University of

Twente. In Chapter 13, the concept behind FC is described along with out-of-band power measurements. In addition to absolute power measurements, in-band and out-of-band spectra need to be obtained via spectrometers for source optimization and to gain a better understanding of the inner workings of EUV sources. A new transmission grating spectrometer is also described for application to EUV sources. In addition to power and spectra, additional plasma measurements are needed to understand ion and electron temperature and density distributions. Chapter 16 covers the topic of plasma diagnostics for EUV plasma sources.

Since the early days of EUVL development, synchrotrons have provided a reliable EUV source for the calibration of mirrors, filters, and detectors. Synchrotrons at NIST, CXRO, PTB, New Subaru, PAL, PSI, and several other institutes have been a much-needed source for calibration. Also, many companies, such as CXRO, PSI and New Subaru, have achieved far more than simple calibration by using synchrotrons for the development of resist, mask inspection, imaging, etc. Chapter 17 covers the key role of synchrotrons in the development of EUVL.

In addition to being generated, photons need to be collected using collector optics while ensuring damage- and debris-free optics. Chapter 14 from Zeiss describes the design, construction, and thermal management of normal-incidence collectors provided for Sn LPP sources for EUVL scanners. While normal-incidence collectors are used in LPP sources, grazing-incidence (GI) collectors are chosen for DPP sources. Chapter 15A describes the design and manufacture of GI optics, while Chapter 15B discusses the application of GI optics for materials processing. The lifetime of these collectors has been a key challenge of EUV sources. Chapters 15C and 15D discuss the interaction of EUV photons and the resulting damage. Chapter 18 covers the important topic of debris mitigation, which thankfully continues to improve giving NI collectors in EUV scanners an extended lifetime.

Lasers have been a key component of EUV sources and lithography, as 193-nm lithography is conducted by excimer lasers as the light sources. Part V (Chapters 19–23) covers the main lasers that are instrumental in today's EUVL and that will be needed for extension of EUVL via the hyper-NA option or Blue-X. Current Sn LPP sources are driven by high-power CO_2 lasers.

Chapter 19 from Mitsubishi describes their design for CO_2 lasers, which have been successfully employed in Gigaphoton's Sn LPP sources. While Cymer's Sn LPP sources use CO_2 lasers from Trumpf, these sources have a different design. Nd:YAG lasers were initially considered as a driver for scanner sources, but power scaling and conversion efficiency caused the industry to choose CO_2 lasers. These lasers still play a role in pre-pulse lasers, leading to the improvement of conversion efficiency (CE) and reduction of debris. In addition, suppliers such as Adlyte are developing LPP sources for

metrology using these lasers as a driver. Chapter 22 from HiLASE covers their Nd:YAG laser development for these lasers. One of the additional lasers that may replace CO_2 lasers as the driver, are the 2-μm thulium lasers from LLNL, described in Chapter 23. These lasers may extend EUVL at 13.5 nm or be used as a driver for Blue-X sources with wavelengths <13.5 nm.

Another laser-based source is high-harmonic-generation (HHG) lasers, which, despite their low power, have found application in EUV mask defect inspection and, in recent years, in resist testing using interference lithography (IL) at Imec. Chapter 21 covers HHG lasers.

As mentioned previously, excimer lasers have been used as a source of photons for 193-nm-based lithography with dry and immersion options. Chapter 20 covers these lasers, as they will continue to play a role in leading-edge lithography, even though more miniscule features are leaning toward EUVL printing in the coming years. To cover all bases, we have included details about DUV lamps, which supported lithography before the advent of 193-nm excimer-based lithography (Chapter 26). Larger back-end features will continue to be printed using these photon sources, while front-end features are moving from 193 nm to EUV wavelengths, then to EUV high-NA and beyond.

Earlier, I mentioned synchrotrons as sources of EUV photons due to their involvement in calibration and R&D. An entire chapter (Chapter 24) is devoted to the basics of synchrotrons. These sources cannot be used for powering the scanners due to their low power. However, FELs have been considered as the next option for providing even higher EUV power to scanners. Until recently, FELs were considered the leading option for power extension in EUVL scanners; however, steady progress in Sn LPPs has removed the focus on this technology for scanners for now, as Sn LPPs are currently fulfilling industry requirements. However, in the longer term, power requirements will only increase. Industry continues to work on FELs—a topic covered in Chapter 25.

I want to remind readers that the previous book on this topic, *EUV Sources for Lithography* will remain a valuable reference, as not every topic within it could be presented in the current volume. We have republished the Xe and Sn emission tables, but only for several topics (i.e., physics of DPP, metrology, and additional types of EUV sources), so readers are encouraged to review the corresponding chapters in that book.

This has been my largest book project ever. This volume contains significant contributions from many individuals and groups working for universities, national labs, consortia, and private companies. Recently, one of my esteemed colleagues, who was once skeptical about the feasibility of EUV lithography's ability to extend Moore's law, called an EUVL scanner a "pinnacle of human engineering." If that is true, then EUV sources are certainly the crown jewel of that achievement. This technology stands as an

amazing achievement that is open to admiration both on the technical front and owing to the successful collaborations among various groups. EUV sources are now widely utilized to manufacture the components of some of the most advanced computer chips in the world.

I would like to thank reviewers Prof. Gerry O'Sullivan and Dr. Klaus Bergmann for their comments and helpful suggestions for improving this Preface and Phylicia Walker (EUV Litho, Inc.) for copyediting it.

Vivek Bakshi
EUV Litho, Inc.
Austin, Texas, USA
July 2023
Vivek.bakshi@euvlitho.com
www.euvlitho.com

Chapter 1
Photon Source Technology for Lithography and Metrology: An Overview

Vivek Bakshi
EUV Litho, Inc., Austin, USA

1.2.4 Current status and future challenges

Current Sn LPP sources from ASML have been able to support EUVL scanners at >250 W. The current lifetime for collectors and the availability of sources (uptime) is also reported to be in an acceptable range. A large increase in the EUVL scanner uptime was achieved via a new design for feeding tin to the droplet system, and the collector lifetime was improved via continued development towards controlling and cleaning tin debris.

Increasing the source power to 800–1000 W is the current main challenge for EUVL scanner sources, a process that will greatly support the throughput requirements of EUVL scanners at future nodes. So far, the results for Sn LPP sources driven by CO_2 lasers[13] have been promising. The increased demand for EUV source power leads to an increase in power from CO_2 drive lasers—but these lasers are not very energy efficient with respect to conversion of wall-plug to laser power. However, switching to 2-μm thulium lasers may be beneficial for pre-pulse and main drive lasers.[19] These solid-state thulium lasers (Chapter 23 and Ref. 20) offer a much higher wall-plug-to-photon conversion efficiency (CE), 30% as compared to 3% for CO_2 lasers,[20] and have the potential to be the drive-lasers for Sn LPP sources for EUV scanners in HVM.

1.3 EUV Source: Discharge-Produced Plasma (DPP)

1.3.1 Fundamentals of DPP

K. Koshelev[21] has given a comprehensive review of EUV photon generation in discharge produce plasmas (DPP). DPP uses electrical energy to generate plasma to produce EUV photons. The mechanism of heating the seed material (xenon or tin) via magnetic compression is called the *pinch effect*. Magnetic field B is generated by current I in the discharge plasma, which then compresses and heats the plasma (Fig. 1.6). The compression stops when the magnetic pressure equals the plasma pressure, as given by Bennett relation, given below:[21]

$\mu_0 I^2/4\pi = (Z_{\text{eff}} + 1)N_i kT_e$ or it can be given numerically as

$$(Z_{\text{eff}} + 1)N_i T = 3.12 \times 10^{21} I^2, \tag{1.3}$$

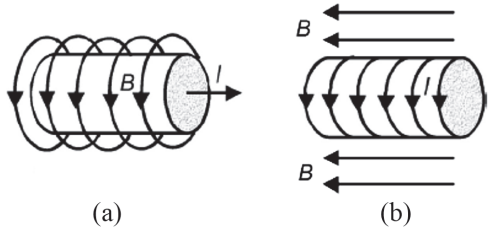

Figure 1.6 Geometries for a DPP (a) liner or z-pinch and for (b) θ pinch. (Reprinted from Ref. 21).

compact and generally less expensive than LPP sources. However, if DPP sources continue to be the favored option for metrology applications, they will need improved power scaling and brightness.

1.4 Atomic Data for Sn and Xe Sources

The choice of 13.5 nm was based on the selection and availability of ML mirrors at 13.5 nm. Xenon, tin, and lithium were all candidate source materials for EUV sources due to their ability to emit photons in the desired wavelength region (see Fig. 2.2 in Ref. 9). But in today's industry, only Sn and Xe are being used. In the end, Sn LPP has been the primary choice for scanner sources. Xe DPP sources [Energetiq (Chapter 8), ILT sources (Chapter 10), and Research Instrument (RI) sources (Chapter 11)], Xe LPP sources,[18] Sn DPP sources (Chapter 9), and Sn LPP sources (Adlyte,[16] ISTEQ,[17] and others) are being used for metrology applications. The optimal source for actinic patterned-mask inspection (APMI) metrology tools has yet to be finalized.

In order to understand the physics of EUV sources, fundamental atomic data for Xe and Sn is needed to improve the performance via modeling and experiments. For xenon, the ionic stage of Xe^{+10} (alternatively noted as Xe XI or ten times ionized Xe atom) is primarily responsible for emissions in 2% bw around 13.5 nm (see Fig. A.2. in Appendix A at the end of this book for an example of emission from Xe ions around 13.5 nm). Appendix A provides the fundamental data for xenon ions.

The ions Sn^{8+}–Sn^{14+} with their resonance transitions $4p^6 4d^m$–$4p^5 4d^{m+1}$ and $4d^m$–$4d^{m-1}4f$ ($m = 6$–0), in particular, are important for the emission of EUV light (see Section 4.1 and Fig. 4.1). Figure 4.1 shows that the relative contribution of tin ions in stages of Sn^{+9}–Sn^{+13} contributes to emission around 13.5 nm. Recent work by Versolato et al. (Chapter 4) has further improved the understanding of atomic data for Sn ions and their relevant EUV applications. In addition, Appendix B provides the fundamental atomic data for tin ions and is reproduced (like Appendix A) from a previous monograph on EUV sources.[4]

Combined with radiation-hydrodynamic models, atomic data is used to model the performance of Sn LPP (Chapters 3 and 5). Several codes are being used to model Sn LPP that sometimes give varying results. Hence, a "Code Comparison" workshop was launched in 2020 to measure the various codes. Results are made available through the official workshop proceedings,[22] and a summary of the comparison has been published as part of proceedings.

1.5 Other Photon Sources

EUV sources have continued to evolve in terms of technology and power to support EUVL scanners, metrology, and the testing needs of the industry.[4,11,22]

Chapter 2
Laser-Produced Plasma Sources for Short-Wavelength Applications Including Lithography and Microscopy

Gerry O'Sullivan and Padraig Dunne
University College Dublin, Ireland

Takeshi Higashiguchi
Utsunomiya University, Japan

Takanori Miyazaki, Fergal O'Reilly, and Emma Sokell
University College Dublin, Ireland

the expansion and uniformity of the initial plasma. With droplet targets, it has been observed that the overall CE increases from 3% to almost 5% if the pre-pulse duration is reduced from 10 ns to 10 ps.[52] For 10-ns pre-pulses on a droplet, the plasma is essentially disc shaped, with the dominant expansion orthogonal to the incident beam direction, while for 10-ps illumination, the plasma is 'dome'-shaped and the expansion is greater in the laser beam direction, meaning that the main pulse interacts with a larger, less-dense volume with a less-steep plasma gradient, which reduces reflection losses.

As mentioned above, if a Nd:YAG pre-pulse is employed, the laser energy is absorbed in, or in front of, the critical density region where the electron density is $10^{21}\,\mathrm{cm}^{-3}$, and reheating is better accomplished with a longer-wavelength laser for better coupling with the lower-density expanded plasma. Commercially available sources use CO_2 lasers to provide the main pulse. The maximum CE calculated for a dual Nd:YAG/CO_2 irradiation scheme is 6.5% into 2π sr for laser energy into in-band energy.[34] The maximum CE available was calculated to be 11.5% for $\Phi = 8\times10^9\,\mathrm{Wcm}^{-2}$ at $\lambda = 10.6\,\mu\mathrm{m}$, with a laser absorption radius of 150 μm during 1–2 ns in a more realistic situation.[32] Since commercial CO_2 lasers have significantly longer pulse lengths, the CEs typically observed are in the range of 4–5%. However, using CO_2 pre-pulses and main pulses, where the pre-pulse deforms the droplet to form a thin disc, a CE of 6% has been demonstrated with very careful tuning of the laser and illumination conditions.[53] The maximum CEs attainable as predicted by comprehensive plasma simulations are discussed in more detail in Chapter 5.

In order to ascertain the maximum CE attainable in a real-world situation, the stagnation layer formed by two identical colliding plasmas produced initially by two equal energy pulses from a Nd:YAG pre-pulse laser was used to provide a target plasma for reheating by a CO_2 pulse.[54] The seed plasmas were formed on a wedge target so that they approached each other essentially at 90 deg by a Nd:YAG laser with $E \sim 135\,\mathrm{mJ}$ in each pulse, focused to $\Phi \sim 1.0\times10^{11}\,\mathrm{Wcm}^{-2}$. The CO_2 pulse was focused to $\Phi = 1.7\times10^9\,\mathrm{Wcm}^{-2}$. When allowance was made for the mismatch between the CO_2 focal spot and the smaller plasma size, a CE of ~7% was inferred. Thus, it would appear that there is scope to increase the maximum CE obtainable in commercial sources by further tailoring of the laser irradiation conditions and droplet dynamics.

2.4 Spectroscopic Observations

2.4.1 Effect of configuration interaction (CI) on Sn UTA emission

In Sn 13.5-nm source plasmas, the ion stages involved all possess a partially occupied $4d$ subshell, and the dominant emission arises from $4p^6 4d^N – 4p^5 4d^{N+1} + 4d^{N-1}4f$ transitions. These transitions overlap in adjacent ion stages to form the well-documented Sn UTA. A UTA can be considered as

which require less energy for their excitation than the $4d$–$4f$ UTA.[102] It is clearly evident from this figure that satellite transitions of the type $4f^{N-1}nl$–$4f^{N-2}5gnl$ in addition to resonance $4f^N$–$4f^{N-1}5g$ must be accounted for, given that they make a contribution to the spectra that is comparable to contribution of the resonance transitions. At shorter wavelengths, the structure due to $4d$–$5p$ and $4d$–$5f$ transitions was also identified. Similar transitions in a number of high-Z elements, including Re, Au, Pt, and Pb, have been reported,[65,103–105] so these elements are potentially usable as short-wavelength sources. In particular, peaks in the $4f$–$5g$ emission from Re and Pt match the Cr/Ti and Cr/Sc MLM reflectivity characteristics quite well.

2.5.3 Blue-X sources based on $\Delta n = 1$ UTAs

As already mentioned, the $4f$–$5g$, $\Delta n = 1$ transitions in Bi were noted to be less susceptible to opacity effects than the $\Delta n = 0$ $4d$–$4f$ UTA. This is to be expected since $\Delta n = 1$ transitions move to higher energy with increasing ionic charge, so emission from an ion with charge $q + 1$ will lie to the shorter-wavelength side of the UTA emitted by an ion of charge q and will not be attenuated by absorption due to the lower charge state. Emission from a number of promising UTAs has been found in spectra from LPPs of second-transition-row elements whose soft x-ray emission is dominated by $3d^N$–$3d^{N-1}4p$ and $3d^N$–$3d^{N-1}4f$ transition arrays, and a number of close coincidences can be found between their peak positions and those of available MLMs.[106] For example, the spectrum of Mo plasmas recorded with a 170-ps laser pulse focused to a 40-μm spot diameter is presented in Fig. 2.12. An analysis of the spectrum indicates that $3d^4$–$3d^34p$ transitions in Mo XXI, $3d^6$–$3d^54f$ transitions in Mo XIX, and $3p^63d^4$–$3d^34f$ transitions in Mo XXI lie close to the reflectance peaks of the three MLM families shown in Fig. 2.12. A useful attribute is that the individual UTAs are broadened by contributions from satellite transitions of the type

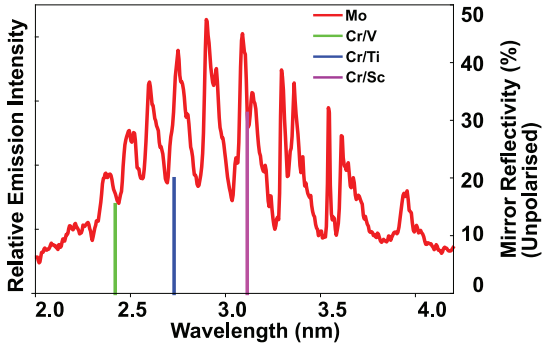

Figure 2.12 Position of reflectance peaks of MLMs and emission of a Mo plasma in the water-window spectral region. Note that better matching can be obtained with a Mo plasma than with nitrogen line emission.

Chapter 3
Radiation-Hydrodynamics Modeling of LPP EUV Sources

Howard Scott, Steven Langer, and Yechiel Frank
Lawrence Livermore National Laboratory, Livermore, California, USA

3.1 Introduction

The use of laser produced plasmas (LPPs) as sources of EUV radiation for lithography is now established for high-volume manufacturing, albeit after a long gestational period. Currently available LPP sources can reliably provide 250 W of 13.5-nm wavelength light with a high duty factor from tin plasma driven by CO_2 laser light. The physical mechanisms underlying the plasma production and EUV radiation are well understood. However, the design and optimization of such sources remains mostly a matter of engineering and experimentation with minimal computational input.

One reason for this is that physical understanding is not easily translated into a computational tool capable of accurately predicting for a given source the quantity desired for use in lithography: radiation within the wavelength window of $13.5 \pm 1\%$ nm. This specific task is particularly difficult for

nonthermal distribution heavily centered around a particular wavelength. Calculating the photon distribution then requires a kinetic treatment, i.e., radiation transport, which is discussed in Section 3.3.

3.3 Laser Absorption

Two of the physical processes critical to this method of EUV production arise from the interaction of light and matter—laser absorption and radiation transport. Although similar at a fundamental level, these processes are modeled with different numerical approaches specialized to handle particular aspects of the interactions. Both methods utilize geometrical optics, i.e., raytracing, rather than wave mechanics to describe light propagation, assuming that the wavelengths are much smaller than relevant spatial scales. The differentiation between the two processes is due to the photon energies and directionality, both of which impact the interaction with plasma.

The laser wavelengths under consideration here vary from 1 to 10 μm, corresponding to photon energies on the order of 0.1 to 1 eV. In this energy range, atomic transitions tend to be much weaker than those in molecules, liquids, or solids. The dominant absorption mechanism in a plasma consisting of ionized atoms is then provided by interactions with free electrons, i.e., inverse bremsstrahlung. However, these photon energies are too low to ionize atoms directly or to eject electrons from metals, so additional absorption mechanisms are required to address low-temperature conditions.

In neutral gases, higher-order interactions allow the laser photons to ionize the matter. The electric field from multiple photons can either directly ionize an atom or modify the atomic potential enough to allow ionization by electron tunneling.[6,7] The laser intensity required for this to occur is quite modest, and once this process has started, inverse bremsstrahlung will quickly dominate the absorption process.

The lasers are also highly directional, making it important to include refraction to follow the direction of propagation for each laser ray incident on the plasma, and refractive effects can control the absorption near the critical surface.

Considering a plasma consisting of ions and free electrons, with motion damped by collisions between electrons and ions with collision frequency ν_c, the dielectric constant of the plasma is given by

$$\varepsilon = 1 - \frac{\omega_p^2}{\omega^2 + i\omega\nu_c}. \tag{3.7}$$

This provides an expression for the (real part of the) refractive index χ:

of EUV transitions. This shortcoming may manifest in the RH evolution because the grossly different optical depth spectrum can affect the overall energy balance through radiation transport. The other atomic models should produce similar optical depth effects and energy balance but would differ dramatically in the emission in the 2% bandpass (gray bar).

However, for a complex atom like Sn, it is not possible to confidently identify the ionization balance and radiative energy loss for any single set of conditions of interest for EUV generation, much less for the wide range of conditions encountered during a RH simulation. The best available calculations are expected to be accurate, although experimental validation is often lacking, and when present, is rarely unambiguous. A possible measure of confidence in the atomic modeling comes from a series of workshops with comparisons of independent CR calculations for specified sets of conditions. Sn under conditions relevant to EUV production was considered in a 2004 workshop[32] focused on NLTE atomic kinetics and, more recently, in a workshop specifically addressing EUV simulations.[33]

A key issue for RH simulations employing NLTE calculations is the effect of radiation fields on the plasma properties. Radiation fields enter through the radiative rates in Eq. (3.31), directly changing the populations involved and indirectly affecting the ionization balance and other properties. A radiation field can dramatically change the emissivity from a set of transitions, or even across the entire spectrum.[26,34,35] The challenge posed to RH simulations is that the local radiation field is determined non-locally by plasma conditions across an extensive spatial domain.

3.7 Radiation Transport

Unlike ions and electrons, photons do not equilibrate quickly and can have very long mean free paths. Radiation transport is then used to evolve the photon distribution in space and time, most commonly as an equation for the specific intensity I_ν:

$$\frac{1}{c}\frac{\partial I_\nu}{\partial t} + \vec{\Omega}\cdot\nabla I_\nu = -\alpha_\nu I_\nu + \eta_\nu = -\alpha_\nu(I_\nu - S_\nu), \tag{3.32}$$

where we have neglected scattering and introduced the source function,

$$S_\nu = \frac{\eta_\nu}{\alpha_\nu}, \tag{3.33}$$

which, in LTE, equals the Planck function. The specific intensity is related to the photon phase space distribution function f_ν by

$$I_\nu = 2h\nu\left(\frac{\nu}{c}\right)^2 f_\nu(\vec{r},\, \nu,\, \vec{\Omega},\, t), \tag{3.34}$$

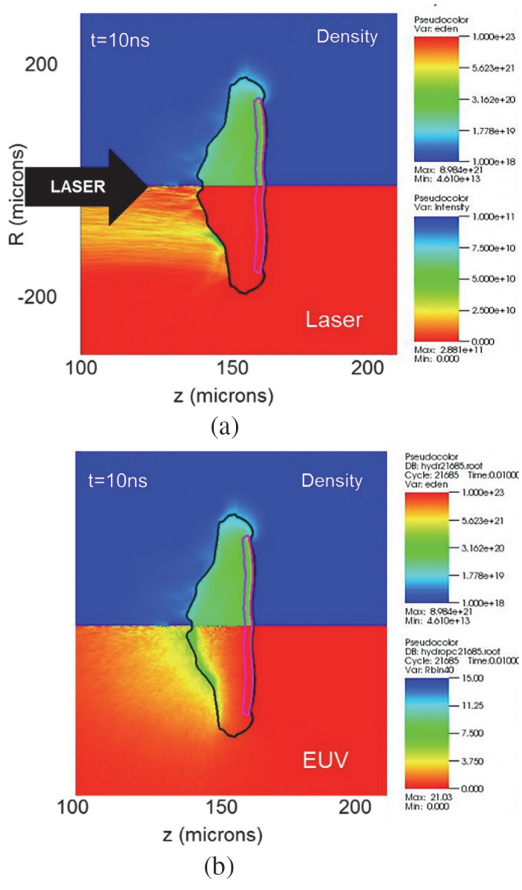

Figure 3.9 Simulations of the main-pulse laser interaction with an expanded disk-like target. Maps of the radial distribution of electron density along the laser axis, 10 ns into the main-pulse laser are shown in the top half of parts (a) and (b). The bottom half of part (a) shows the main-pulse laser rays traveling through the dense plasma. The bottom half of part (b) shows the corresponding EUV emission. (Reprinted from Ref. 44.)

The main laser pulse quickly heats and ionizes this vapor. Interaction of the main-pulse laser with an expanded disk-like target and EUV emission produced 10 ns into the main pulse are shown in Fig. 3.9.

3.10 Future Trends

Now that 13.5-nm light from Sn has become a mainstream EUV source, lithographic atomic physics research has shifted to producing shorter-wavelength light through the use of different materials.[46,47] The first challenge for producing useful simulations will lie in obtaining and using high-fidelity atomic data. Since temperature and density regimes will not change significantly, the scalings inherent in Eq. (3.6) demonstrate that NLTE

4.1 Introduction

Multiply charged tin ions in laser-produced plasma (LPP) are bright emitters of extreme-ultraviolet (EUV) light near 13.5-nm wavelength as used in state-of-the-art nanolithography.[1–4] Such plasma is produced when molten Sn microdroplets are illuminated by energetic laser pulses. The ions Sn^{8+}–Sn^{14+} with their resonance transitions $4p^6 4d^m – 4p^5 4d^{m+1}$ and $4d^m – 4d^{m-1} 4f$ $(m = 6 – 0)$,[3–5] in particular, are important for the emission of EUV light (see Fig. 4.1). Spectroscopic investigations of Sn LPPs are challenging as there are many closely spaced transitions in the various contributing Sn ions. Spectral transition arrays belonging to adjacent ionic charge states effectively blend in wavelength and produce an unresolved transition array (UTA).[6–8]

Most spectroscopic works have had to deal with the simultaneous EUV emission from several tin charge states as sustained by the various plasmas.[12–22] Nevertheless, the works on, e.g., discharge plasma sources to date provide the most accurate spectroscopic data in the EUV. More recently, a challenge was provided to this EUV data by charge-state-resolved optical spectroscopies of magnetic dipole transitions of tin ions bred and

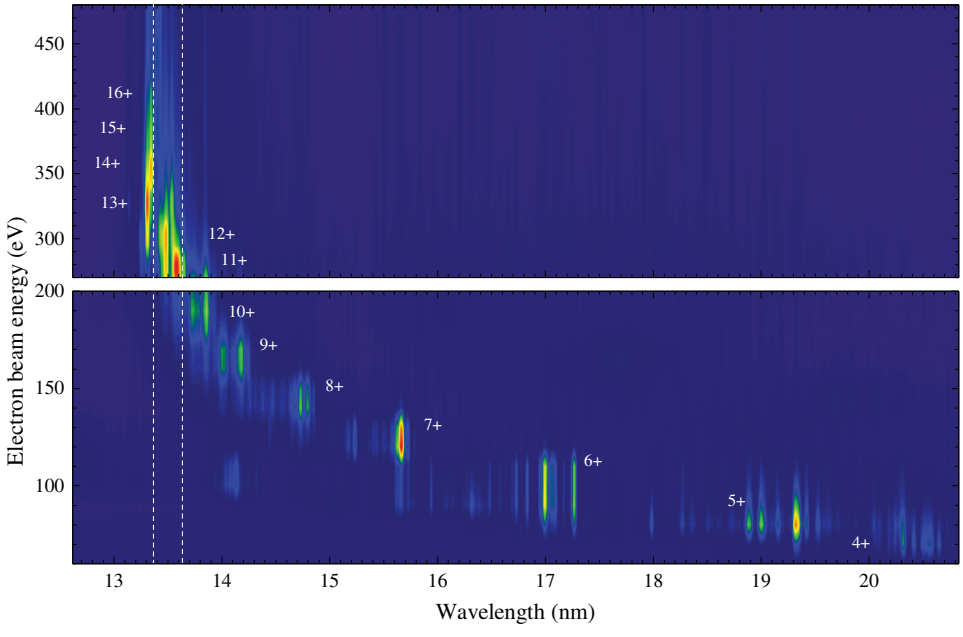

Figure 4.1 Spectral intensity map of Sn ions constructed from measurements at the FLASH-EBIT.[9] The 2D map is produced by interpolating spectra taken at set electron beam energy steps. The main features belonging to the various Sn^{q+} multiply charged ions (with charge q) are labeled. The dashed vertical lines indicate the 2% bandwidth around 13.5-nm wavelength relevant for nanolithography. (Figure, adapted from Ref. 10, is based on data presented in Refs. 9 and 11, with permission from authors.)

of the opacity is accounted for by higher-lying transitions, of which 26% is attributed to transitions between singly and doubly excited states, 25% to transitions between doubly and triply excited states, and 38% is associated with higher excitations.[28] Zooming in on the opacity in the application-relevant 2% bandwidth, we find that the resonance transitions are seen to account for only 19% of the opacity. The data that support the findings of this study are available from the corresponding authors upon reasonable request.

4.2.4 Comparison to experiment

To benchmark the calculations, we next provide comparisons (as originally presented in Ref. 28) with experimental data from laser-produced micro-droplet-tin plasmas. ATOMIC calculations were performed at predicted ranges of plasma temperatures and densities, and were subsequently compared to experimentally obtained spectra. This enabled identifying the conditions that lead to best agreement between modeling and experiment. The experiment itself is described in detail in Ref. 27 (also see the detailed discussion on EUV source metrology in Chapter 13). The selected spectra were recorded at three distinct Nd:YAG laser intensities (see Fig. 4.6). Next, to be able to compare atomic opacity calculations to experimental emission spectra, the authors of Ref. 28 adopted a strongly simplified approach of 1D radiation transport in a single-temperature, single-density plasma. Recent experiments performed by Schupp et al.[39,40] have indicated that EUV emission spectra may be quite accurately captured in this manner (see Section 4.4 for further details on the model). The temperature of the calculated opacities was chosen such that the calculated charge-state contributions were commensurate with observed short-wavelength out-of-band spectral features.[25,26] The choice of specific density and path length scales was justified from radiation hydrodynamic simulations using the RALEF-2D code;[35,36,41] see Ref. 28 and see Chapter 5 for further details on the RALEF-2D code. In the current comparisons, a constant 30-μm path length at 10^{20} e^{-}/cm^{-3} electron density was used.

Figures 4.6(a)–(c) present a comparison of the experimentally obtained spectra with spectra obtained from the 1D radiation transport model in which the ATOMIC opacity calculations serve as required input, as obtained from Ref. 28. Overall, the level of agreement is excellent. The results are compared with calculations from previous works in Fig. 4.6(a) (see Ref. 28 for further details). The relevance of the multiply excited states is seen to decrease with decreasing plasma temperatures, although their contribution is still required for complete opacity spectra.

4.3 Maxwell–Boltzmann Statistics in Non-LTE Plasma

The assumption of LTE conditions can be useful for interpreting and understanding radiation losses from dense plasmas, as was demonstrated in

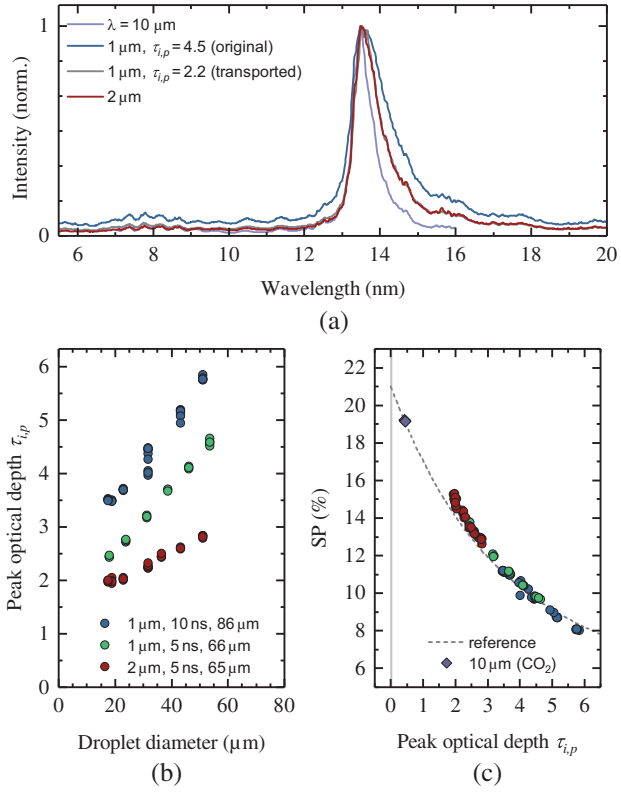

Figure 4.13 Experimental results on optical depth scaling from experiments on tin microdroplet plasma.[40] (a) Spectrum produced using 2-μm wavelength drive laser light, shown as a solid red line, is compared to the 1D-radiation-transported reference spectrum (gray line) taking $\tau_p = 2.2$. For further details see Ref. 40. Also shown is a spectrum obtained using a 10-μm CO_2 laser to irradiate tin microdroplets in an industrial setting.[97] (b) Peak optical depth $\tau_{i,p}$ as a function of droplet diameter for 5- and 10-ns laser pulse duration at 1-μm wavelength and for 4.3-ns pulse duration at 2-μm wavelength. (c) Experimental SP values as a function of $\tau_{i,p}$. The dashed line presents the SP values from the radiation-transported reference spectrum (see main text); the diamond symbol indicates the SP value for $\tau_{i,p} = 0.4$, obtained from comparison to the EUV emission spectrum of the CO_2-laser-driven plasma. (Figures adapted from Ref. 40.)

tables—of plasma generation using even longer-wavelength laser systems between 2- and 10-μm—would enable finding truly optimal conditions to drive LPP for generating 13.5-nm radiation for next-generation EUV nanolithography.

4.5 Conclusion

Multiply charged tin ions brightly emit EUV radiation near the 13.5 nm wavelength in laser-produced plasma. The relevant tin charge states include Sn^{8+}–Sn^{14+}. These ions radiatively contribute not only with their well-known

Chapter 5
Radiation-Dominated Plasma in LPP Sources: Physical Aspects and Challenges for Numerical Modeling

Mikhail M. Basko
Keldysh Institute of Applied Mathematics (KIAM), Russian Academy of Sciences, Moscow, Russia

For our purposes, the use of the diffusion approximation is reasonably well justified because the main effect of intense thermal radiation on the ablation flow is produced through the reabsorption zone (see Section 5.4.5), where the inward-bound emitted flux impinges on the oncoming dense and cold ablated material and is fully absorbed therein; as a result, the thickness of this zone is always either comparable to or larger than the effective mean free path of photons. The two radiation variables S_r and J_r remain continuous across the discontinuity at $x = x_2$. The boundary conditions for Eqs. (5.22) and (5.23) are

$$S_r(x_0) = J_r(x_0) = 0, \tag{5.24}$$

$$S_{r2} \equiv S_r(x_2) = 3^{-1/2} J_r(x_2). \tag{5.25}$$

Equation (5.25) is the Hopf–Bronstein relation,[42] which is exact in a gray planar atmosphere with a constant radiative flux. Note that, by its physical meaning, the outgoing radiation flux S_{r2} is non-negative and must be calculated as the eigenvalue of the boundary-value problem formulated in Eqs. (5.22)–(5.25). In combination with the boundary conditions given in Eqs. (5.19)–(5.21), Eqs. (5.13)–(5.15) yield

$$\rho u = j = \sqrt{\gamma p_2 \rho_2}, \tag{5.26}$$

$$p + \rho u^2 = p_a = (\gamma + 1) p_2, \tag{5.27}$$

$$w_2 + \frac{u_2^2}{2} = \frac{\gamma(\gamma+1)}{2(\gamma-1)} \frac{p_2}{\rho_2} = (1 - \phi_r) \frac{I_L}{j}, \tag{5.28}$$

where $\phi_r = S_{r2}/I_L$ is the fraction of the incident laser flux carried away to $x = +\infty$ by the thermal radiation.

5.4.4 Scaling laws for the ablation parameters

Under the assumption that the fraction ϕ_r of radiative losses is known, Eqs. (5.26)–(5.28) allow the ablation rate j, the ablation pressure p_a, and the corona temperature T_2 be calculated without knowing the structure of the ablation front—provided that the relation between ρ_2 and T_2 is fixed by the condition $n_e = n_c$. The latter is justified insofar as the laser absorption in the underdense corona is negligible.

To evaluate the coronal laser absorption, we make use of the Kramers formula[43] for the inverse-bremsstrahlung absorption coefficient k_L in the limit of $\hbar\omega_L \ll T$, cast in the following form:

$$k_L = k_{Lc} \left(\frac{n_e}{n_c} \right)^2, \quad k_{Lc} = 1.08 \times 10^5 \frac{z_i \ln \Lambda_L}{T_{eV}^{3/2} \lambda_{L,\mu m}^2} \text{cm}^{-1}, \tag{5.29}$$

correspond to the lowest possible value of the parameter $a_{uv} = 1$, i.e., to situations where the master pulse is almost fully absorbed just before the critical surface, and the working zone lies immediately above it. Plasma configurations with $a_{uv} > 1$, where the master pulse encounters a very shallow density gradient and is fully absorbed in the far underdense corona, are inefficient because of the inevitable strong reabsorption of the in-band EUV photons in the working zone. Remarkably, this conclusion is virtually independent of the master-laser wavelength λ_{mL} and of the steepness of the radial density profile represented by index n. So long as the optimal temperature T stays close to 30 eV, the ratio τ_{uv}/τ_{mL} is confined to a limited range of $\tau_{uv}/\tau_{mL} \approx 0.3$–$0.6$.

The above considerations lead to the following general logic of the optimization procedure for attaining maximal CE. Once the wavelength λ_{mL} of the master laser is fixed, the asymptotic density profile [Eq. (5.72)] is characterized by a single parameter R_{mc} (hereafter we assume that $n = 2$). For any fixed value of R_{mc}, one carries out one-parameter optimization with respect to the master-laser irradiation intensity I_{mL} to determine the optimal plasma temperature T. Then, by varying R_{mc}, one establishes the absolute maximum of CE.

The fact that CE must have a maximum as a function of R_{mc} becomes evident after one supposes that, for different R_{mc} values, the optimal value of T undergoes little variation. Indeed, because τ_{uv} and τ_{mL} are both proportional to R_{mc} and $a_{uv} \geq 1$, R_{mc} values that are too low imply low CEs because $\tau_{mL} \ll 1$ and the laser is poorly absorbed; in the opposite limit, R_{mc} values that are too high lead to $\tau_{uv} > 1$ and quenching of the in-band emission due to its self-absorption.

Equation (5.71) tells us that, for a fixed value of λ_{mL}, variation of the source size R_{mc} can be achieved by changing either the droplet radius R_d, or the wavelength λ_{sL} of the slave laser, or both; variation of the slave-laser intensity I_{sL} to this end makes little sense because of the weak dependence of R_{mc} on this parameter. The inverse temperature dependence in Eq. (5.77) suggests that the effects of departure from LTE (or from steady-state ionization equilibrium due to rapid transit through the working zone), which typically require higher T values to attain the same ionization states z_i, should lead to somewhat higher optimized CEs than those obtained in the LTE (or a quasi-stationary non-LTE) approximation.

5.5.4 Results of optimization

The results of the full two-parameter (R_{mc}, I_{mL}) optimization are presented in Table 5.4, where different columns list the one-parameter optimization results obtained by varying I_{mL} for different fixed values of R_{mc}. The values of R_{mc} were progressively increased by increasing the droplet radius R_d in combination (for the last column) with a reduction of λ_{sL}. The intensity of

Chapter 6
EUV Sources for High-Volume Manufacturing

[This chapter was originally published as Chapter 3A in *EUVL Lithography, Second Edition*, V. Bakshi, Editor, SPIE Press Vol. PM283 (2018). It has not been updated here.]

Igor V. Fomenkov, David C. Brandt, Alexander I. Ershov, Alexander A. Schafgans, Yezheng Tao, and Georgiy O. Vaschenko
ASML US, San Diego, USA

Bruno La Fontaine
Hermes Microvision Inc., an ASML company, San Jose, California, USA

6.1 Introduction to EUV Light Sources

This chapter describes the development of a laser-produced-plasma (LPP) EUV source for advanced lithography applications in high-volume manufacturing (HVM) of semiconductor devices. EUVL is expected to succeed 193-nm immersion multi-patterning technology for sub-10-nm critical-layer patterning. The most recent results from high-power systems targeted at the 250-W configuration are described to date. The requirements

stannane molecules, thus reducing the effects of Sn re-deposition due to stannane dissociation. The total Sn cleaning rate is thus

$$K_{\text{net}} = K_{\text{SnH}_4\_\text{formation}} \cdot (1 - K_{\text{Sn\_redep}}), \quad [6.4]$$

where K_{net} is the net etch rate of Sn, $K_{\text{SnH}_4\text{–formation}}$ is the rate of SnH_4 formation, and $K_{\text{Sn\_redep}}$ is the rate of Sn redeposition.

Another application that hydrogen is used for is protection of the scanner volume (illumination optics) from debris generated in the source. The scanner has many optical surfaces that are very expensive to replace and are very sensitive to contamination. Primary micro-particles generated at the plasma location are usually blocked by a small obscuration in the direct line of sight from the plasma to the IF. This way, virtually 100% of all primary debris can be blocked from traveling into the scanner volume. There is, however, still a risk of secondary debris penetrating the scanner. This risk is minimized by careful design of the internal hardware of the source vessel. As can be seen, hydrogen as a buffer gas provides several functions for Sn management, the most important being reduction of Sn flux to the collector, etching Sn from the collector, cooling the plasma region, and carrying debris out of the vessel. It is clear that hydrogen is the leader by a large margin for all three functions; thus, hydrogen is the best gas to use in the LPP source.

An alternative method to reduce the Sn flux moving toward the collector can be achieved using magnetic confinement. Gigaphoton developed the concept of magnetic debris mitigation. The idea of this concept is to trap Sn ions with a strong magnetic field and direct them into a designated Sn trap, as shown in Fig. 6.48.[37] A fairly high magnetic field (exceeding 1 T) is required, thus necessitating use of superconducting magnets. Also, in order for this concept to be efficient, reduced background gas pressure is required; otherwise, collision of Sn ions with gas molecules will reduce the efficiency of the magnetic field trapping.

Figure 6.49 shows a plot of the reported debris deposition onto the collector with magnetic debris mitigation.[38] Sn flux is quite small for most of the collector surface, but in two locations it reaches about 2 nm per Mpulse, which is near the location of the traps. This is a very high flux that cannot be easily cleaned and will likely mean quick loss of EUV reflectivity in these areas. Overall, magnetic debris mitigation can be considered as an alternative or addition to the baseline debris mitigation with hydrogen gas.

6.3.7 Tin management

Besides keeping the collector free from debris, another important issue is properly managing tin accumulation in the vessel. The problem is very challenging due to the volume of Sn used by the source. A simple calculation assuming 50-kHz operation of the source with a 20% dose margin and 80%

droplet is either inside or outside the beam path. This works throughout an exposure because the scanner moves the wafer beneath the illuminating slit until the entire die has been illuminated. Every point on an exposure field is exposed to EUV light for an amount of time equal to the time required to move that point through the slit, which can be as short as 5 ms (or 250 shots). The amount of EUV light received by each point on the field is given by a (weighted) moving average of the pulse-to-pulse EUV energy, also known as the dose. Thus, PCM is able to regulate the average EUV energy during wafer exposure so that every die on the wafer is exposed (dosed) with the same amount of EUV energy. This technique requires that the source be capable of generating an average EUV energy per pulse larger than the desired target energy by 20–30%. This energy overhead is required so that all packets can achieve their average energy target. Pulse count modulation is capable of generating a stable EUV dose on the order of 0.2%.[16]

6.4 Summary and Future Outlook

With scalability to meet requirements of ASML scanners, laser-produced plasma sources have been shown to be the leading technology and provide a path toward the higher power needed by lithography tools as they evolve over their life cycle. Five NXE:3100, eight NXE:3300B, four NXE:3350B, and two NXE:3400 BLPP sources have been used by leading-edge chipmaker R&D sites around the world, accumulating the necessary knowledge and know-how to eventually move into the HVM environment. MOPA pre-pulse technology has been validated as the path to higher power output, and stabilized power of 250 W at intermediate focus has been demonstrated, using advanced control technology to meet the dose stability target of $<\pm 0.5\%$ 3σ with reduced dose margin. Normal-incidence collector mirrors with $>$5-sr light collection and high average reflectivity are being produced in volume and are showing increasingly long lifetimes in the field. Enhanced collector protection and *in situ* cleaning technologies are both expected to further increase lifetime. Several more NXE:3400B sources are currently being built and are planned to be shipped to customers in 2017.

References

1. R. Peeters, S. Lok, E. van Alphen, N. Harned, P. Kuerz, M. Lowisch, H. Meijer, D. Ockwell, E. van Setten, G. Schifflers, J.-W. van der Horst, J. Stoeldraijer, R. Kazinczi, R. Droste, H. Meiling, and R. Kool, "ASML's NXE platform performance and volume introduction," *Proc. SPIE* **8679**, 86791F (2013) [doi: 10.1117/12.2010932].
2. D. C. Brandt, I. V. Fomenkov, A. I. Ershov, W. N. Partlo, D. W. Myers, N. R. Böwering, N. R. Farrar, G. O. Vaschenko, O. V. Khodykin, A. N. Bykanov, J. R. Hoffman, C. P. Chrobak, S. N. Srivastava,

Chapter 7
EUV Light Source for Lithography

Hakaru Mizoguchi, Akira Endo, Yutaka Shiraishi, Tatsuya Yanagida, Shinji Nagai, Takashi Suganuma, Krzysztof M. Nowak, Georg Soumagne, Hiroaki Nakarai, Yoshifumi Ueno, Takashi Saito, and Toshihiro Oga
Gigaphoton, Inc., Kanagawa, Japan

7.2.5 Driver CO_2 laser system

An EUV power level of 115 W at IF was initially drawn as the minimum value required to enable HVM-worthy productivity of 100 wafers/hr. Once all sources of EUV photon loss located between the plasma and the IF had been accounted for, the HVM productivity target required ~500 W of EUV power at the plasma point.[31] Such an EUV power level at the plasma, in turn, required at least 18 kW of average drive-laser power delivered in stable pulses of repetition rates in excess of 50 kHz. More recent estimates are that >330 W at IF is needed; therefore, there is continuing pressure for development of a more powerful laser driver.[9]

Theoretical and experimental studies[32–35] have shown that the ~10-μm wavelength generated by CO_2 lasers is more favorable for a LPP EUV source than the ~1-μm wavelength delivered by solid-state lasers in terms of higher CE and reduced production of debris.[36,37] An optimal timescale for energy coupling from the laser field to the plasma was found to be around 10 ns for CO_2 lasers.[38] Traditionally, the pulsed operation was achieved either by gain-switching, intracavity *Q*-switching, passive or active mode-locking, or extra-cavity modulation (Fig. 7.16). However, only the electro-optical modulation methods could provide the required pulse format and sufficient control to facilitate synchronization with the Sn droplet target.

The first account of an electro-optically modulated, cavity-dumped, *Q*-switched technique is believed to be reported in 1963,[39] and an application to CO_2 lasers was made not so long after that.[40] This configuration, depicted in Fig. 7.16, combined with cw-like radiofrequency (RF) pumping, could realize the required pulse repetition rates and a pulse duration of 10–20 ns, delivered in a relatively good temporal shape, as shown in Fig. 7.17. This kind of master oscillator, employing a sealed-off, RF-discharge-excited, waveguide laser was used previously in LPP EUV source development.[41–43] However, the output power level was limited in this kind of master oscillator to <20 W; therefore, post-amplification was required to reach multi-kilowatt powers, forming the configuration of a so-called master oscillator–power amplifier (MOPA) system.

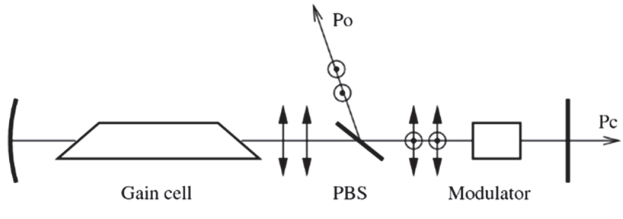

Figure 7.16 Schematic of a conventional *Q*-switched cavity-dumped pulsed laser (PBS is polarizing beam splitter, P_o is output power passing the transmitting flat mirror, and P_c is coupled power as the modulated output) (reprinted from Ref. 60 with permission from IEEE).

7.4 High-Power HVM LPP-EUV Light Source Development

7.4.1 Gigaphoton LPP EUV light source

7.4.1.1 System overview

The HVM EUV light source layout of Pilot #1 from Gigaphoton Inc. (GPI) is shown in Fig. 7.50. Pilot #1 consists of a drive laser system, a beam transfer system, and a EUV chamber system. To realize this EUV light source system, GPI has been operating three prototypes of EUV light sources: Proto #1, Proto #2 and Pilot #1. As shown in Table 7.6, the major difference between

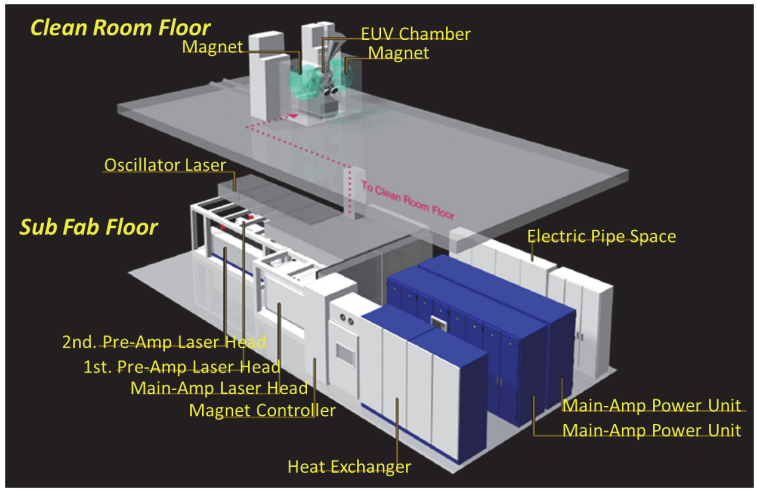

Figure 7.50 GL200E-Pilot #1 diagram (reprinted from Ref. 93).

Table 7.6 Target specification of Gigaphoton's EUV light sources.

		Pilot #1 Proof of Concept	Proto #2 Key Technology	Pilot #1 HVM Ready
Target performance	EUV power	25 W	>100 W	250 → 330 W
	CE	3.0%	4.0%	5.0 → 6.0%
	Repetition rate	100 kHz	100 kHz	100 kHz
		Horizontal	62 deg (upper)	62 deg (upper)
Technology	Droplet diameter	20–25 μm	20 μm	20 μm
	CO_2 laser power	5 kW	20 kW	26 kW
	Pre-pulse laser pulse width	picosecond	picosecond	picosecond
	Chamber cooling and gas flow	25-W level	125-W level	330-W level
	Collector mirror lifetime	Use as a development platform	10 days	>3 months

Chapter 8
The Electrode-less Z-pinch Metrology Source

Stephen Horne, Deborah Gustafson, Matthew J. Partlow, Wolfram Neff, Michael Roderick, and Kosuke Saito
Energetiq Technology, Inc., Wilmington, USA

8.1 Introduction

The original EQ-10 electrodeless inductive Z-pinch EUV source has evolved in various directions, driven by customer demands. A high-frequency version (10 kHz instead of 3 kHz) was required for mirror testing. Experiments with helium addition elucidated the stability behavior of the source. In a non-EUV application, a version was produced to generate light at 2.88 nm, for use as a water window microscope illuminator. Some data at 6.7 nm has also been obtained. This chapter reviews the operating principles of the source and describes the performance in various applications.

To be useful as a microscopy illuminator, the source must meet certain requirements. Since the microscope uses a zone plate as an objective lens, the illuminating light must be substantially monochromatic to avoid chromatic aberration. Source brightness must be sufficient to provide an image in a reasonable time—minutes at most. Maintenance requirements should not be onerous or require significant downtime.

Nitrogen was chosen as the radiating gas. Helium-like nitrogen radiates strongly at 2.88 nm, which is essentially a perfect wavelength for the application. The source of this radiation is helium-like nitrogen in the $1s2p$ state at 426–430 eV. Radiation from hydrogen-like helium is possible at 2.48 nm (500 eV) but is conveniently blocked by a 300-nm Ti filter, which has a strong absorption edge at 2.73 nm (454 eV).

8.7 Spectral Measurements

During the proposal phase of this project, we assembled a home-made spectrometer. The spectrometer used a 200-nm period grating and 25-μm slit as a dispersive element. Instead of using an entrance slit or pinhole to improve resolution as is done in commercial instruments, an astronomical spectrometer was imitated by using a long evacuated tube as a beam line between the source and the grating—thus, the plasma appeared as a very small star-like source. This expedient allowed the collection of surprisingly good spectra at the cost of long integration times. The detector was a Peltier-junction-cooled back-thinned CCD camera.

Figure 8.11 shows the zero-order peak and the two first-order spectra obtained from a nitrogen plasma. The horizontal scale is in units of nanometers and is based on the grating and camera geometry; the origin is chosen to be at the location of the zero-order peak. The y axis is in units of counts from the camera.

Figure 8.12 shows the detail of the spectrum of nitrogen in the water window at 2.48 and 2.88 nm. The spectrum has been "folded" to overlay the $+1$ and -1 orders; nominally, the curves should be identical and overlay perfectly. The difference gives some idea of the noise level in the signal. The line identifications are taken from R. Lebert et al.,[20] who identify the line at 2.879 nm as a helium-like transition, $1s^2$–$1s2p$. The transition at 2.49 nm is identified as helium-like, $1s^2$–$1s3p$, while the 2.478-nm feature is identified as a hydrogen-like transition, $1s$–$2p$. In fact, since the feature at 2.879 nm is due to a helium-like transition, we would expect the line to be a doublet formed of two lines with transition energies of 426 and 431 eV (2.904 nm and 2.879 nm.) The raw spectrum implies that somewhat more power is available at the lower energy line at 430 eV (2.88 nm) compared to the feature at 500 eV (2.48 nm).

The spectral data shown above were taken with an early prototype source, as part of our proposal to NIH to fund the source work. That

Chapter 9
High-Brightness Laser-Assisted Discharge-Produced Plasma EUV Source for Mask Inspection and Exposure Applications

Yusuke Teramoto
Ushio Germany GmbH, Aachen, Germany

increase the measurable wavelength region, an aluminum mirror, placed in front of the thermopiles at the incident angle of 45 deg, was used as well. The 45-deg aluminum mirror was used to cut the radiation of $\lambda = \sim 60$ nm. Six data obtained with two measurements (with and without the aluminum mirror) were analyzed, taking into account the spectral transmissions of the filters and the aluminum mirror.

Figure 9.17(a) shows the ratio of radiation power to total radiation power in five different wavelength regions. More than 90% of the total radiation is in the region $\lambda = 10$–20 nm. About 4% is in the region $\lambda = 20$–130 nm, and less than 1% is in the region $\lambda > 130$ nm. Figure 9.17(a) was further processed to derive a spectral intensity distribution, as shown in Fig. 9.17(b), taking the bandwidth of each filter into account. This spectral distribution is somewhat like the simulation in Ref. 21, which is a simulation on a tin droplet LPP source with a $\lambda = 2$ mm laser. Although this experiment did not have a spatial resolution, previous research suggests that most OOB radiation originates from the electrode surfaces.[30]

9.5 Source Stability and Reliability

9.5.1 Source brightness stability

For any EUV applications that include mask inspection, the source stability is one of the important factors in evaluating source performance. Figure 9.18 shows EUV brightness stability measured with an EUV camera, in which the exposure time was 1 ms, when the source was running at 10 kHz in a constant-voltage mode. The data of 5 min in this case show that there was no significant

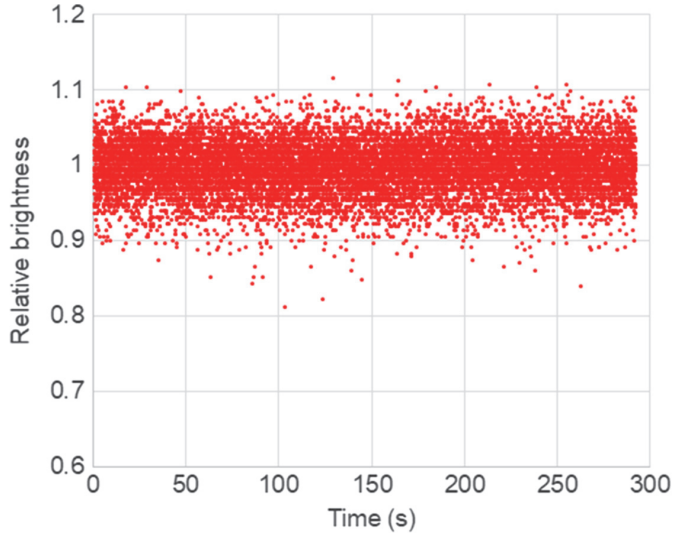

Figure 9.18 Relative brightness variation measured with an EUV camera at 10 kHz.

Chapter 10
Compact EUV Sources for Metrology and Irradiation Experiments

Klaus Bergmann, Jochen Vieker, and Alexander von Wezyk
Fraunhofer Institute for Laser Technology (ILT), Aachen, Germany

Florian Melsheimer
Institute of Semiconductor Nanoelectronics, Forschungszentrum Jülich, Germany

10.1 Introduction

Dense and hot plasmas are well known as efficient sources of extreme ultraviolet (EUV) or soft x-ray radiation. Such plasmas can be generated in compact systems, where matter is heated to high temperatures, either by electrical energy or absorbed laser radiation. The preferred channel for energy losses is radiative transitions, which is the key to a high overall conversion

10.3 Source-Collector Module

10.3.1 Basic considerations

The incoherent emission of plasma-based EUV sources is, to a first approximation, isotropic. For efficient use of the emitted radiation, a collector is required, which gathers the light and focuses it onto a sample or into an optical system—to a position that is often referred to as the intermediate focus (IF). Each application will lead to specific requirements at the intermediate focus. The collector must be designed to fulfil these requirements for the source under consideration and minimize the required source power or maximize the achievable photon flux at the IF. Other aspects such as debris mitigation, collector lifetime, or spectral filtering must be considered in addition to the collector module design, itself. In general, the situation for the source-collector design can be simplified as is shown in Fig. 10.17. Some requirements will be imposed by the application, which mainly include the average intensity I, the spot size d, and the allowed opening angle at the sample position Ω_{sample}. Note that the scheme is also valid for collectors operating near normal incidence. The collector module requirements can be reduced to two parameters: the magnification M and the overall transmission T_{coll}. The overall transmission includes the reflectivity of the optical element as well as the optical transmission of the debris mitigation system and of additional spectral filters. With such simplification, the minimum required average source power can be written as (recalculated for the emission into 2πsr) follows:

$$P \geq 2\pi \frac{1}{T_{\text{coll}}} M^2 \frac{1}{\Omega_{\text{sample}}} \pi \left(\frac{d}{2}\right)^2 I. \tag{10.12}$$

Note that the magnification does not necessarily refer to an imaging element, but rather to the ratio of the entrance solid angle to the exit solid angle, with $M^2 = \Omega_{\text{coll}}/\Omega_{\text{sample}}$. For the given requirements on the focal parameters, this formula suggests minimizing the collector magnification as

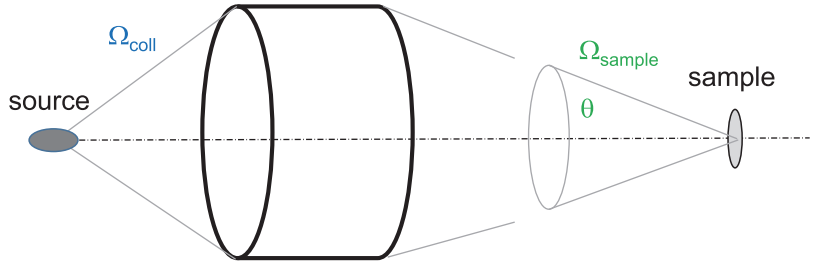

Figure 10.17 General scheme of a collector for gathering and focusing of the isotropic light emitted from the plasma onto a spot in the focal plane. The spot size is dependent on the plasma extension and the solid angle for the entrance and exit of the collector.

Chapter 11
The EUV-Lamp: A Discharge-Produced Metrology EUV Source

Rainer Lebert, Christoph Phiesel, Thomas Missalla, and Andreas Biermanns-Föth
RI Research Instruments GmbH, Bergisch Gladbach, Germany

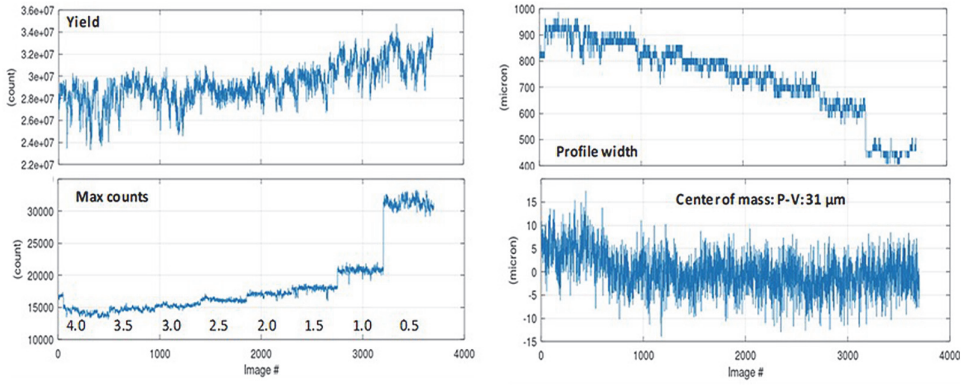

Figure 11.33 Profile variation with alternating bias-gas flow setting, where the lowest N_2 bias results in the highest brightness.

11.3.7 Lifetime/mean time between failures (MTBF)

EUV-Lamps in the field routinely reach electrode lifetimes above 400 million source pulses (about 2000 hours operation at 50 Hz). Some of them work in batches of more than 80 hours of permanent emission. So far, no distinct lifetime limit of the electrodes has been observed. However, after these 400 MPulses, the pulse-to-pulse fluctuations slightly increase. When refurbished-discharge melt areas are observed on the anode, a borehole extension with material deposited around it is seen on the cathode, as shown in Fig. 11.34.

Usually, we suggest routine source head refurbishment after these 300 MPulses, often finding the electrodes to be fully operational without any traces that would indicate that the end of its lifetime is approaching (see Fig. 11.34). Ultimately, end of life is reached when boreholes are widened so much that the emission volume loses its axial symmetry, or the hollow-cathode effect for ignition fails. It should be noted that the MTBF lies in the

Figure 11.34 Status of electrodes after more than 300 million discharge pulses: (left) cathode, (center) gap facing the side of the anode, and (right) exterior of the anode.

Chapter 12
Laser-Driven Plasma Source Technology and Applications

Huiling Zhu, Toru Fujinami, Xiaohua Ye, Don McDaniel, and Deborah Gustafson
Energetiq Technology, Inc., Wilmington, Massachusetts, USA

12.1 Introduction

Broadband radiation sources with ever-increasing radiance are sought after by semiconductor applications in various processes. It is well known that plasmas make excellent light sources due to their broadband emission throughout the UV/VIS/IR wavelengths. Over 40 years ago, Yu. Raizer started investigating laser-driven continuous optical discharge (COD) using mid-IR 10.4-μm CO_2 lasers, providing the initial technical understanding of laser-driven plasmas (LDPs).[1] It took the convergence of two separate elements: (1) the availability of lower-cost and high-efficiency near-IR (NIR) (~1 μm) high-power diode

Chapter 13
EUV Source Metrology

Muharrem Bayraktar
University of Twente, The Netherlands

Fei Liu
ASML Netherlands B.V., Veldhoven, The Netherlands

Oscar Versolato
Advanced Research Center for Nanolithography (ARCNL), The Netherlands and
Vrije Universiteit Amsterdam, The Netherlands

Fred Bijkerk
University of Twente, The Netherlands

Chapter 14
Normal-Incidence Collector Optics for EUV Sources

Sascha Migura, Tobias Müller, and Frank Hartung
Carl Zeiss SMT GmbH, Oberkochen, Germany

14.1 Introduction

As a crucial component of the EUV source, the collector optics is a precisely polished mirror that collects the EUV light emerging from the plasma and focuses this light into the output aperture of the source vessel, the so-called intermediate focus (IF) (see Fig. 14.1). The whole EUV optical system within the scanner consists of ten or more mirrors. The EUV optical train starts with the collector mirror, which provides light for the illuminator module in a defined way at the IF; the position of the IF must be kept stable in space and a certain opening angle and orientation must be met and also be kept stable. The IF is followed by mirrors in the illuminator module, which illuminate the mask. The optical train ends with the mirror group of the projection optics. The total transmission of these optical submodules determines how much EUV power emitted by the plasma can be used for imaging of chip structures onto the wafer. On each of the above mirrors, usually a multilayer coating is applied that reflects the EUV light. The optical constants of available coating

a point on the surface of the collector mirror to the secondary focus is a direct function of the radial distance to the optical axis. For a larger radial distance, the reflectance of the collector decreases. Consequently, the collector far field is not homogeneous, which results in the typical far-field intensity profile as shown on the right in Fig. 14.3. The far field is characterized by a maximum reflectance zone near the optical axis and a decrease in intensity towards the edge of the collector mirror. Due to the rotational symmetry of the ellipsoidal mirror, the far field is circularly symmetrical, the center hole being a consequence of the physical hole in the ellipsoidal mirror through which the infrared (IR) laser beam enters the system. In addition, cut-outs in the far field occur because of the tin droplet supply parts, which cut off a certain rectangular-shaped section of the far field (see the left side of the far-field intensity given in Fig. 14.3). These inhomogeneities and obscurations are compensated by the illumination optics: The field and the pupils generated by the illumination optics feature a uniform and homogeneous intensity distribution.

14.4 Wavelength Spectrum and Reflectivity

A broad wavelength range of intense electromagnetic radiation hits the collector mirror.[22] As the source plasma is powered by the strong IR drive laser that hits the tin droplets, multiphoton ionization of the target material occurs during the first phase of the laser pulse as the electromagnetic field increases. The electric field of the laser pulse further accelerates the free charges, and the free particles exchange kinetic energy with each other through collisions. On this basis, a dense and strongly ionized plasma is created that tends to expand. The tin atoms can be ionized several times, and finally the plasma reaches the recombination state in which the generation of EUV radiation is made possible. At some point, the laser light will no longer penetrate the plasma and will be reflected from the plasma surface. Therefore, the IR laser light is not completely absorbed by the tin droplets and thus reaches the collector surface together with the EUV radiation. A wide variety of wavelengths is generated in the plasma. The plasma spectrum is the result of various emission processes, ranging from the emission of free electrons to the recombination of ions, atoms, or molecules. These different processes happen at different spatial and temporal development stages in the plasma and each lead to different emission wavelengths and wavelength bands. The LPP plasma spectrum thus covers wavelength bands from soft x-ray (a few nanometers) to the IR (several microns). Each of these wavelengths can feature very different conversion efficiencies. The resulting emission spectrum of the plasma is typically divided into specific wavelength bands to enable distinguishment of the different effects on the lithography process:

Chapter 15B
Materials Processing with Focused EUV/Soft-X-ray Pulses

Kazuyuki Sakaue
The University of Tokyo, Japan

Light in the EUV/soft x-ray wavelength region can be well focused due to its short wavelength and has high absorption for all materials. Such features make it possible to realize precise and efficient materials processing. In this chapter, direct materials micro-/nanoprocessing using focused EUV/soft-x-ray pulses is introduced as an application using a short-pulsed EUV/soft-x-ray beam obtained by high-order-harmonic generation (HHG) and a free-electron laser (FEL). The processing threshold fluence of materials in the EUV/soft-x-ray wavelength region is about one to two orders of magnitude lower than that of the near-infrared (NIR) or visible-light range, which is the wavelength range of lasers used in the materials-processing industry. The threshold fluence strongly depends on the material, but in general, 10 to 100 mJ/cm^2 for polymer thin films, 50 to 200 mJ/cm^2 for metals, and 100 to 400 mJ/cm^2 for semi-conductors and insulator such as silicon and glass are required for processing. The EUV/soft-x-ray pulse obtained from a FEL has sufficient pulse energy but is relatively low at around the nanojoule/pulse rate in HHG. However, the HHG source is tabletop sized so it is preferable for industrial applications. To achieve sufficiently high fluence for materials processing and to realize direct micro-/nanofabrication, EUV/soft-x-ray pulses must be focused on a submicrometer scale. Using grazing-incidence optics, it is possible to efficiently obtain a focused spot close to the diffraction limit.

material but often occurs due to nonthermal solid-to-solid phase transitions resulting in changes of surface morphology, usually expansion. Some experimental (see, for example, Ref. 27) and theoretical (see, for example, Ref. 28) studies were carried out during the last decade. However, it is difficult, and maybe too early, to summarize and generalize their miscellaneous results in this chapter.

15C.3 Permanent Radiation Damage to EUV Optics

In principle, both reflective and refractive optical elements positioned at various angles of incidence can be used as a part of beamlines and focusing layouts built and operated at modern EUV/x-ray sources. In this chapter, it might seem that we should concentrate only on the damage occurring under grazing-incidence conditions. However, a majority of experimental findings (especially damage thresholds) in the literature are reported for normal-incidence conditions. Therefore, it would be of use to prospective readers of this chapter to learn how to estimate damage thresholds under grazing-incidence conditions (usually at an incidence angle smaller than the critical angle) from experimentally determined normal-incidence damage results (the beam comes to the sample surface along its normal, i.e., perpendicularly to the surface).

Amorphous carbon (a-C) represents a widely used optical coating deposited on high-quality silicon substrates that will serve as large grazing-incidence mirrors for guiding and focusing of EUV FEL beams (see, for example, Ref. 29). To estimate the mirrors' damage thresholds, a magnetically sputtered 890-nm-thick a-C layer on the planar silicon substrate was exposed under angles below, around, and above (up to the normal-incidence case) the critical angle to single ultrashort pulses of FLASH (free-electron laser in Hamburg) radiation.[30] The FEL device was tuned at a wavelength of 7.0 and then 13.5 nm where the a-C coating exhibits a critical angle of 8 deg and 15.8 deg, respectively. Sixty pulses of 13.5-nm radiation were fired against a-C sample at grazing angles equal to 4.3 deg, 15.1 deg, and 18.7 deg. The same number of pulses exposed the sample at 4.3-deg, 7.7-deg, and 10-deg grazing angles by 7.0-nm radiation. The irradiation was also performed under normal-incidence conditions.

Pulse energy was varied by a gas attenuator, and photon flux was measured by an absolutely calibrated gas photoionization detector [gas monitor detector (GMD)]. Damage patterns were analyzed by Nomarski microscopy [also known as differential interference contrast (DIC) microscopy] and atomic force microscopy (AFM) in a tapping mode. Material expansion due to FEL-induced sp^3-to-sp^2 conversion in the all-carbon material represents the key damage mechanism here. The process is considered a kind of graphitization. Therefore, the expansion is caused by the well-known fact that

Chapter 16
Plasma Diagnostics

Kentaro Tomita
Hokkaido University, Sapporo, Japan

16.1 Introduction

Further progress of the practical usage of the EUV lithography technique is dependent on improvement of the plasma diagnostic technique because the chamber of the EUV light-source is filled with various types of plasmas. For example, the light source itself is a dense (10^{24}–$10^{25}\,m^{-3}$), small-sized ($\sim$0.5 mm), and a moderate-temperature (25–50 eV) plasma. Also, EUV-induced photo-ionized hydrogen plasma fills the space between the light source and the EUV collecting mirror. The predicted ranges of electron density n_e and electron temperature T_e are very wide: 10^{16}–$10^{25}\,m^{-3}$ and 0.1–50 eV, respectively. n_e and T_e are fundamental parameters that characterize the plasma. Therefore, these wide ranges of n_e and T_e should be measured as far as is possible. In addition, observation of the Sn target condition before irradiating the main laser is also important because the plasma parameters may strongly depend on the initial tin target condition. Here, the conventional way to produce the EUV sources for high-volume manufacturing is briefly explained. First, microdroplets of Sn are prepared. Second, the droplets are shot with

frequency was determined. Reference 20 shows square-electric-field-weighted volume-averaged n_e values as a function of time for various hydrogen pressures. The energy of an EUV pulse at the IF was fixed at $44 \pm 2\,\mu J$. The EUV-pulse-energy dependency of n_e was also measured. It was concluded that the maximum n_e as a function of gas pressure can be fit by quadratic curves. On the other hand, the maximum n_e was found to be proportional to the EUV energy.

16.4 Ion Diagnostics

Measurements of ion properties is one of the most important points for improving the lifetime of EUV lithography source systems. Laser-produced tin plasmas for EUV light sources produce not only in-band EUV light, but also debris, which consists of droplet fragments, clusters, tin atoms, and ions. Without careful elimination of the debris, the lifetime of the EUV-light-collecting multilayer optics would be short; i.e., tin ions having higher energy that are ejected from the EUV source may cause a serious problem due to their high sputtering efficiency.[22] In order to reduce the damage of the multilayer surface due to the bombardment of energetic particles, H_2 buffer gas is conventionally used. H_2 is available as an ion-stopping gas because its EUV absorption cross-section is very low. The Sn-ion stopping power is determined by the H_2 gas pressure. To determine the optimum H_2 pressure, distributions of the kinetic energy and charge state of the Sn ion should be known.

16.4.1 Charge-averaged ion energy distribution measurements

For the measurement of the ion energy distribution of laser-produced plasmas, Faraday cups (FCs) are usually used due to their robustness and compactness. FCs yield charge-averaged energy spectra from the obtained time-of-flight (TOF) results of the detected current signals. When the FCs are installed at different angles, angular dependencies of the ion energy distribution can be obtained. Typically, EUV sources operate in pulsed mode. In this case, TOF spectroscopy is automatically available using FCs. The principle of the TOF technique is based on a simple relation: the travel time t of charged particles across an already-known distance d is measured. The relation between t and d is expressed as follows:

$$t = d/\sqrt{2E/m}, \tag{16.7}$$

where E is the initial energy of the ion, and m is the ion mass. Namely, this technique provides the E/m ratio of ions emitted from the plasma. If m is already known, the distribution of E is observed by time-resolved measurements.

Chapter 17
Synchrotron-based Metrology Tools for EUV Lithography

Charles Tarrio and Robert E. Vest
NIST—National Institute of Standards and Technology, Gaithersburg, USA

Frank Scholze and Michael Kolbe
PTB—Physikalische-Technische Bundesanstalt, Berlin, Germany

Yasin Ekinci
PSI—Paul Scherrer Institut, Villigen, Switzerland

17.4.2 Detector characterization

17.4.2.1 Self-calibration

AXUV-type photodiodes with nearly ideal responsivity have been proposed as absolute detectors[80] for the EUV spectral range.[68] The basic idea is that the spectral responsivity $s(h\nu)$ of a photodiode for photons of energy $h\nu$ in the soft-x-ray region can be expressed as

$$s(h\nu) = (e/w)s_r(h\nu), \tag{17.2}$$

where e is the elementary charge, w is the mean electron–hole pair creation energy, and $s_r(h\nu)$ a relative responsivity accounting for all loss processes, like reflection and absorption in the front layer. Reflection at normal incidence is negligible in the EUV spectral range. Thus, for an ideal detector with 100% internal charge collection, only the absorption in the front layer needs to be known. This is the basis for an alternative approach to the determination of the spectral responsivity of photodiodes used earlier at PTB in the soft-x-ray spectral range,[81] so-called self-calibration.[82] The absorptance of the front layers can be determined from the ratio $s_\Theta(h\nu)$ of the responsivity for 60 deg to normal to that for normal incidence of the radiation. If only absorption in top layers is considered as the loss process, $s_\Theta(h\nu)$ equals $s_r(h\nu)$ because the path length through these layers doubles under 60 deg to normal. The relative uncertainties were estimated to be about 4% for n-on-p silicon diodes and about 6% for GaAsP Schottky diodes.[81] Later on, this model was extended to account for a thin layer beneath the diode front contact, where the generated charge is only partially collected.[65] The extended model better describes the charge losses in a photodiode and was successfully used to derive the mean energy for the production of electron–hole pairs in semiconductors from the absolutely measured responsivity of photodiodes using the ESR.[65] Measurements in the soft-x-ray range at PTB revealed a quantum efficiency proportional to the photon energy, i.e., a constant value of $w = 3.66(3)$ eV for the generation of an electron–hole pair in silicon in the wavelength range from 0.5 nm to 20 nm. For wavelengths above 330 nm, exactly one electron–hole pair per absorbed photon is created, and for wavelengths shorter than 150 nm, the mean energy per electron–hole pair converges to the constant value for shorter wavelengths.[66,71,77] For GaAsP, a value of $w = 4.58(7)$ eV was measured in the EUV and soft x-ray spectral range.[66]

The relative uncertainty achievable by the self-calibration method, however, is limited by the quality of the optical data used for the calculation of $s_r(h\nu)$ from the measured ratio $s_\Theta(h\nu)$. For the above-mentioned determination of w for silicon, the optical data of the nitrided oxide had to be deduced from reflection measurements. The situation becomes even worse for highly absorbing front layers like gold or silicides. The uncertainty is proportional to $1 - s_r(h\nu)$. For AXUV diodes with nearly ideal responsivity

Chapter 18
Tin Mitigation in EUV Sources

Gianluca Panici and David N. Ruzic
University of Illinois Urbana-Champaign, Champaign, USA

18.1 Introduction

Every day, computers continue to infiltrate all facets of modern life, creating an enormous industry and encouraging innovation. The transistor is the initial invention that kickstarted this phenomenon. Gordon Moore of Intel, during the beginning of this technological movement, stated that every two years the number of transistors on an integrated chip must double to ensure that demand and innovation goals are met. The size of a transistor in 2001 was 0.25 μm.[1] The current industry standard in the 7-nm node is 14 nm for the half-pitch of the fins of the transistors. Technological advances have begun to run into physical constraints, slowing progress below Moore's prediction. Even the fact that the 7-nm node is 7 nm in "name only" when it is more than double that in feature size illustrates the problem.

To increase the number of transistors on a chip, the size of transistor features must decrease accordingly. The transistor manufacturing steps are traditionally called lithography, etching, and deposition. Lithography uses light to pattern a wafer. The patterns are then etched by either a chemical (wet etching) or plasma (dry etching) process. Finally, these patterns are filled by deposition. As both etching and deposition are fundamentally on the atomic

Chapter 19
Compact Efficient CO_2 Amplifiers with Modular Design for High-Efficiency EUV Power Generation

Koji Yasui
Mitsubishi Electric Corporation, Tokyo, Japan

Jun-ichi Nishimae, Tatsuya Yamamoto, and Yuzuru Tadokoro
Advanced Technology R&D Center, Mitsubishi Electric Corporation, Amagasaki City, Hyogo, Japan

19.1 Background of EUV Applications for the United States

In Japan, since the early days of research, university professors and others have been proposing the application of EUV light to next-generation semiconductor lithography. However, the application of EUV lithography to actual semiconductor production lines was postponed many times, and until recently, the common perception in Japan was that EUV lithography would not be used in actual semiconductor production lines. On the other hand, about 10 years ago, the importance of semiconductors began to be discussed in the manufacturing industry with which the authors are associated. At that time,

Chapter 20
Excimer Lasers for Lithography

Hakaru Mizoguchi, Osamu Wakabayashi, Toshihiro Oga, Hiroaki Nakarai, Hiroshi Komori, Kouji Kakizaki, and Junichi Fujimoto
Gigaphoton Inc., Kanagawa, Japan

principle, the power laser works as a self-sustained laser. The oscillation efficiency is higher than in the MOPA operation (Fig. 20.8).

As a brief summary, the technical merits of injection-lock technology allow us to take advantage of several benefits: high efficiency, narrow spectral bandwidth, wide tolerance of timing, very small seed light requirement for operation, and long pulse duration.

20.3 Progress of DUV Lithography

20.3.1 Exposure tool

The most widespread industrial application of excimer lasers has been in DUV photolithography,[13,15] a critical technology used in the manufacturing of microelectronic devices (i.e., semiconductor integrated circuits or "chips"). Historically, from the early 1960s through the mid-1980s, mercury-xenon lamps had been used in lithography for their spectral lines at 436- and 365-nm wavelengths, respectively. However, with the semiconductor industry's need for both higher resolution (to produce denser and faster chips) and higher throughput (for lower costs), the lamp-based lithography tools were no longer able to meet the industry's requirements. This challenge was overcome when, in a pioneering development in 1982, DUV excimer laser lithography was proposed and demonstrated at IBM by Kanti Jain.[13,14,15,18] With the phenomenal advances made in equipment technology in the last two decades, and with today's microelectronic devices fabricated using excimer laser lithography totaling $400 billion in annual production, it is the semiconductor industry's view[17] that excimer laser lithography has been a crucial factor in the continued advance of Moore's law, enabling minimum features sizes in chip manufacturing to shrink from 800 nm in 1990 to 10 nm in 2016.[19] From an even broader scientific and technological perspective, since the invention of the laser in 1960, the development of excimer laser lithography has been highlighted as one of the major milestones in the 50-year history of the laser.[20,21,22]

Excimer lasers are widely used in high-resolution photolithography exposure tools, one of the critical technologies required for microelectronic chip manufacturing. Until 1996, excimer laser high-pressure mercury lamps were used in the UV region, e.g., the g-line (436 nm) and the i-line (365 nm). Current state-of-the-art lithography tools use DUV light from KrF and ArF excimer lasers with wavelengths of 248 nm and 193 nm, respectively (the dominant lithography technology today is therefore also called excimer laser lithography[13,14,15,16]), which has enabled transistor feature sizes to shrink below 45 nm.

ArF immersion lithography was proposed by Nikon in 2002. This technology uses water between the wafer and the final projection lens. The resolution is extended by the refractive index of water $n = 1.437$ (@ $\lambda = 193$ nm).

Chapter 21
Coherent EUV Light Sources Based on High-Order Harmonic Generation: Principles and Applications in Nanotechnology

Henry C. Kapteyn
Kapteyn-Murnane Laboratories Inc., Boulder, USA; and JILA and Department of Physics, University of Colorado at Boulder, USA

Margaret M. Murnane, Yuka Esashi, Michael D. Tanksalvala, Joshua L. Knobloch, and Chen-Ting Liao
JILA and STROBE NSF STC and Department of Physics, University of Colorado at Boulder, USA

Daniel D. Hickstein and Clayton Bargsten
Kapteyn-Murnane Laboratories Inc., Boulder, USA

Kevin Dorney and John Petersen
Imec, Leuven, Belgium

increased efficiency of conversion requires high-quality pulse compression at higher pulse energies than is currently routine. High-energy pulse compression work has a long history[55–57] of slow progress, the incremental pace resulting from the fact that the nonlinearities employed are difficult to control and not in any way self-limiting. Since most published results do not fully characterize peak focusable intensity and spatio-temporal distortions, the effect of these distortions on HHG efficiency inherently has a high degree of uncertainty.

21.4 Nanotechnology Applications

Coherent EUV high harmonics have demonstrated the ability to play an important role in support of nanotechnology and quantum science. EUV light has an intrinsic ability to monitor function, and the femtosecond pulse nature of the HHG source makes it possible to freeze even the fastest dynamics. The excellent spatial coherence also makes these sources ideally suited for a range of new coherent diffraction dynamics and imaging modalities.

In terms of industrial applications of high-harmonic sources, production of integrated circuits (ICs) is a large-scale nanotechnology enterprise, and the inherent resolution and sensitivity associated with short-wavelength light has potential application, for example, in detecting defects in bare wafers or patterned surfaces. Furthermore, the recent introduction of EUV lithography using 13.5-nm light into IC manufacturing creates potential opportunities, for example, for through-pellicle nanoimaging of the masks to review specific areas and to monitor mask condition in production.

21.4.1 Coherent diffractive imaging with 13.5-nm light

Coherent diffractive imaging (CDI) is an emerging collection of techniques that enable high-resolution, phase-sensitive imaging even without imaging optics. Instead of an imaging optic, CDI techniques generally allow the light to propagate freely to the detector after scattering from the sample. As a result, the field at the detector resembles the Fourier transform of the light leaving the sample, as shown in Fig. 21.10. By iteratively enforcing knowledge in the sample space and detector space, these techniques can enable phase-sensitive imaging with diffraction-limited resolution.[58] This eliminates the severe constraints imposed by conventional image-forming optics (typically, zone-plate lenses) that have previously limited resolution to $\sim > 5\,\lambda$.

While simple implementations of CDI can work well, they are often sensitive to noise and imperfect knowledge of the experiment. A CDI technique known as ptychography is able to overcome these limitations to some degree and is rapidly gaining popularity.[59] In this scheme, a coherent beam is focused successively onto several overlapping regions of the sample, and at each region, a diffraction pattern is recorded. This overlap provides inherent redundancy in the collected dataset and offers improved reliability in

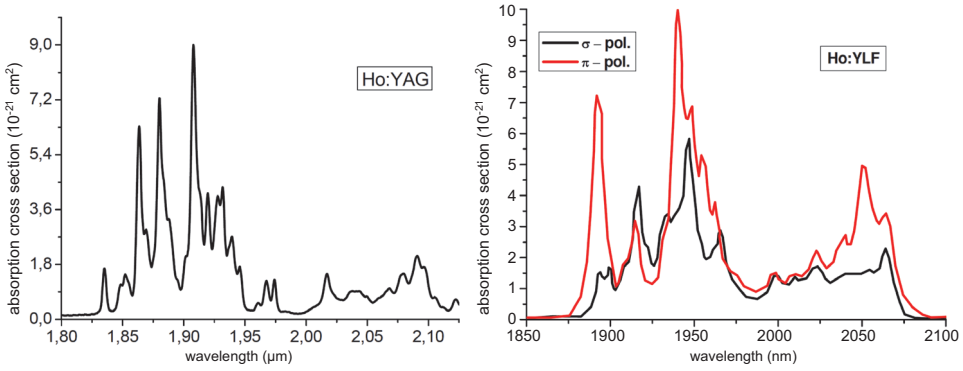

Figure 22.18 Absorption cross-sections of (left) Ho:YAG and (right) Ho:YLF gain media (reprinted from Ref. 85).

However, co-doped crystals are not favorable for high-power laser operation. Nowadays, Ho ions are effectively pumped by high-power continuous-wave Tm lasers. They offer a nearly diffraction-limited beam quality and a very narrow emission bandwidth. The wavelength of fiber lasers can be tuned to the maximum absorption of the holmium ions by using fiber Bragg gratings (1908 nm). Due to these benefits, the highest slope efficiencies for in-band pumped holmium lasers were achieved with thulium fiber lasers as pump sources. The maximum absorption in Ho:YAG can be found around 1908 nm (absorption cross-section $= 9 \times 10^{-21}$ cm^2), and the corresponding line bandwidth is 7 nm. For Ho:YLF, the maximum absorption depends on the polarization; for π polarization, the maximum is at 1940 nm (Fig. 22.18). Emission of Ho:YAG is maximal at 2090 nm with an emission cross-section of 12.9×10^{-21} cm^2 and a saturation fluence of 5.1 Jcm^{-2}. The lifetime at the upper laser level approaches 9.2 ms.[85]

Ho-doped lasers show great potential for the in-band pumping of holmium crystals. Maximum continuous-wave output powers of up to 100 W and maximum pulse energies of up to 50 mJ were demonstrated. The achieved slope efficiency of 80% with the fiber laser pumping shows that there are no significant upconversion losses for in-band pumping. Additionally, lately, several high-power thin-disk lasers[89,90] and thin-disk oscillators[91,92] generating 400-fs-long pulses have been demonstrated.

22.5 Laser Pulse Generation and Amplification

Most of the high-power pulsed lasers work in a MOPA scheme, where a high-quality seed beam is amplified in one or more power amplifiers. This approach enables high stability, high beam quality, and high pulse energy, regardless of the pulse duration. The master oscillator is the most frequently a Q-switched nanosecond laser or a mode-locked picosecond or femtosecond

22.7.6 Post-compression of ultrashort pulses

A further increase in pulse peak power can be realized via controlled employment of a nonlinear Kerr effect (self-phase modulation). For high-power lasers including thin-disk lasers, pulse spectrum broadening in a gas-filled Herriott cell was demonstrated.[188,189] Picosecond pulses from high-power Yb:YAG lasers can be broadened to a sub-100-femtosecond pulse duration in this way. The Herriott cell is a resonator-like system consisting of two spherical mirrors that define the beam size and power density in the nonlinear medium. In addition, the mirrors are designed to have a nonzero anomalous dispersion, compensating the newly induced nonlinear phase between two Herriot cell roundtrips. Such a system enabled the compression of the output pulse from a Yb:YAG disk laser to 40 fs.[190] The pulse energy was as high as 18 mJ. Post-compression of higher-energy pulses is difficult because of ionization problems. In moderate energy systems, post-compression via thin slabs of solids (fused silica, YAG, or another material) was demonstrated.[191] In the case of a Yb:YAG thin-disk oscillator, a combination of a Herriott cell together with spectral broadening in slabs allowed for the generation of 27-fs-long pulses from Yb:YAG.[165] Because the next energy increase from thin-disk lasers is complicated and approaches the technological limits, the peak power increase from Yb:YAG lasers by post-compression is a very promising approach.[192]

Alternatively, regenerative amplifiers can be carefully designed in such a way that the spectral broadening can be induced directly in the cavity, for example, in a Pockels cell crystal, instead of by post-compression. Such an approach can amplify an ultrashort pulse immediately during the amplification process, eliminating the need for passive spectral broadening and thus reducing losses.[152,154]

22.8 Kilowatt-Class Pre-pulse Picosecond Yb:YAG Laser System: PERLA®

The compact thin-disk kilowatt-class laser platform PERLA® is being developed in-house at the HiLASE Center.[1,2] The PERLA® laser has plenty of applications in industrial picosecond laser micromachining applications, including applications in EUV lithography, where such a laser serves as, for example, a pre-pulse laser for preheating of tin droplets. The PERLA® platform is based on a high-power regenerative amplifier aiming for 1 kW of average output power in the most advanced configuration. A similar concept was reported by Trumpf Scientific.[140] The PERLA® platform can currently be optimized for high repetition rates ranging from 1 kHz to 200 kHz, which is sufficient for a majority of the target applications. Alternatively, the platform can be extended to include a thin-disk multi-pass amplifier, enabling for, for example, burst mode operation.[188,193,194]

Chapter 23
Solid State 2-μm Laser Drivers for EUV Lithography

Brendan A. Reagan, Thomas Galvin, Issa Tamer, Emily Sistrunk, Thomas Spinka, and Craig W. Siders
Lawrence Livermore National Laboratory, Livermore, USA

23.1 Introduction

Light sources for extreme-ultraviolet lithography (EUVL) have recently entered high-volume manufacturing (HVM) for the critical layers of the most advanced integrated circuits. These sources implement pulsed, multi-tens of kilohertz repetition rate, radiofrequency (RF) discharge-driven CO_2 lasers at a wavelength of $\lambda = 10.6\,\mu m$ to heat expanded liquid Sn droplets to a temperature and density where strong emission of incoherent $\lambda = 13.5\,nm$ light occurs.[1] Initially, the EUV community examined a number of alternative drive lasers, including diode-pumped ~1-μm solid-state lasers (SSLs), but robust, high-power, moderately efficient, industrial RF-pumped CO_2 lasers were well-established and exhibited the greatest laser-to-EUV conversion efficiency among the lasers tested, which led to early standardization of CO_2

arrays. Following this general architecture, detailed designs—including the pump area and slab dopings—were generated using the procedure given in Ref. 77.

For quasi-monochromatic laser operation, the ~1880-nm peak on the π-axis of Tm:YLF should be employed to benefit from the high gain, particularly at low temperatures, due to the reduced re-absorption and increased emission cross-section amplitude. As an additional benefit, the thermal properties (thermal conductivity, thermal expansion, and thermal lens) of Tm:YLF improve with temperature.[69]

23.4.4 Pulse shaping and repetition rate versatility

Output pulse shapes are constrained by gain distortion in SPE amplifiers, which must extract a significant amount of the stored energy within the gain medium to operate efficiently. As the upper-state population is depleted upon amplification of the seed pulse, the gain is reduced. Consequently, the tail end of the pulse, which interacts with the gain medium after the gain has been saturated by the peak of the pulse, experiences lower gain. This effect would tend to distort a pulse that was initially flat in time at the input into a shape with a sharp initial peak, which slowly tails off. While it is possible to compensate for gain distortion by sculpting the shape of the extraction pulse before it enters the amplifier, there are dynamic range limitations and not all output pulse shapes are readily feasible.

MPE amplifiers do not suffer from significant gain distortion, since only a relatively small fraction of the upper-state population is depleted with each shot. As a result, the gain experienced by the tail of the pulse nearly equals that experienced by the leading edge. Complex input-pulse shapes are therefore directly mapped to the output with little distortion of the shape due to gain saturation. In addition to the complex sculpting of a single pulse, pre-pulses can easily be added with little distortion in the relative magnitudes and shapes of both the pre-pulse and the main pulse.

Figure 23.8 displays the low square-wave distortion nature of amplification in MPE-type amplifiers. In Fig. 23.8(a), a complex, double-peaked pulse shape is mapped with little distortion from the input to the output of the amplifier. Figure 23.8(b) shows the amplification of two independently sculpted pulses in quick succession. Note that distortion is small both inside each sculpted pulse and in the magnitude of the two pulses. This feature makes MPE-based architectures particularly attractive for driving EUV sources, as the impacts of pulse duration[84–86] and pulse shape[87] have been shown to be critical factors in CE.

Another unique feature of MPE-based amplifiers is the ability to operate a single amplifier over a range of output pulse energies and repetition rates. When the repetition rate is much greater than the inverse lifetime of the gain material ($PRF \gg 1/\tau_{storage}$), the storage efficiency saturates near unity and

Chapter 24
Accelerators and Compact Storage Rings for Lithography and Metrology

Yasin Ekinci, Terence Garvey, Andreas Streun, and Leonid Rivkin
Paul Scherrer Institute, Villigen, Switzerland

24.1 Introduction

Accelerator technology is used to generate light of high brightness at short wavelengths, which is then employed to study matter and its physical and chemical reactions. Although it is extensively used for academic research, and research institutes operate the facilities, its commercial applications have been

24.5.6 Requirements for metrology applications

For any type of metrology application, the brightness of the source is the main performance parameter. Given that the overhead time for sample preparation and loading is negligible, and there are no other time-limiting factors (such as detector or stage), the throughput is proportional to the source brightness. This is primarily the case for short wavelengths, i.e., the EUV, soft-x-ray, and hard-x-ray regimes, where generation of light with high brightness is more difficult.

The brightness requirements for EUV metrology for semiconductor applications depend on the specific application as well as on the optical approach chosen to address the specific application. For EUV actinic mask metrology, three specific tools are needed during the fabrication and quality assessment of EUV masks. These tools have been identified as critical to support the mask infrastructure: actinic mask blank inspection (ABI), aerial image measurements (AIMS) and defects review, and actinic patterned mask inspection (APMI). The specifications for these tools were reported by a common discussion of the tool suppliers a decade ago.[44] However, semiconductor manufacturing has continuously moving targets, and these specifications are subject to frequent updates. For all three of these applications, brightness is still the key factor. Other factors that are also important include étendue, intensity stability, pulse repetition rate, pulse duty cycle, and availability.

The required brightness values for ABI are reported as higher than 30 W/mm^{2}sr.[45] For AIMS, the minimum brightness required is 30 W/mm^{2}sr and ideally higher than 100 W/mm^{2}sr.[46] For APMI, the values reported in the literature vary from 20 to more than 1000 W/mm^{2}sr.[44,47,48] In a more recent and detailed study, clear guidelines are provided for the source brightness, and a minimum brightness of 10–50 W/mm^{2}sr is reported.[49] However, this requirement highly depends on the defect sensitivity, detector pixel number, étendue, and throughput requirements. In certain cases, the required brightness exceeds 300 W/mm^{2}sr. The required source power is reported as 1–100 mW, depending on the detector pixel size, photon count per pixel, and throughput. It should be noted that these requirements on power and brightness will increase for future technology nodes, which will require higher resolution and sensitivity. Since the brightness requirements scale quadratically with sensitivity and resolution, a brightness of more than 1000 W/mm^{2}sr will ensure the requirements of future technology nodes.

In addition to the full-field imaging techniques mentioned above, coherent diffraction imaging (CDI) is also an emerging technique that has been demonstrated for EUV mask metrology by many groups.[50–52] The brightness and flux requirements of this technique are subject to more unknowns. Even for the well-established full-field imaging methods, the estimations can vary by two orders of magnitude. For a relatively new method of CDI, it is quite

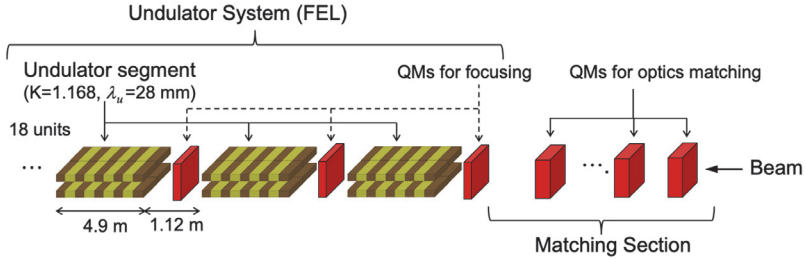

Figure 25.16 Undulator system and optics-matching section (QM: quadrupole magnet).

circularly polarizing undulator has a larger FEL-parameter value than a linear-polarizing undulator, but also because circularly polarized light is more suitable for EUV lithography systems developed for LPP sources that radiate unpolarized light than linearly polarized light. However, various polarization states including circular and linear polarization can be generated by using variably polarizing undulators, such as an Apple-II type[36] undulator. From this point of view, ERL-FELs are highly extendable and advantageous. The segment gap length is about 1 m, and a focusing quadrupole magnet, a phase shifter, and vacuum components are placed in the segment gap. The phase shifter controls the path length of the electron bunch by a magnetic chicane in order to correct the phase difference between the undulator radiation and the electron bunch. The optics-matching section is placed in front of the undulator system to optimize the Twiss parameters at the FEL entrance. The focusing strength of the quadrupole magnets between the undulator segments should be also optimized for maximizing the FEL output power. The beam energy slightly and gradually decreases in the undulator system by radiating the EUV-FEL light. The undulator tapering is performed by changing the magnetic gaps of the undulator segments according to the decrease in the beam energy to increase the FEL output power.

25.3.7 Performance

A start-to-end (S2E) simulation using particle tracking and FEL codes can estimate the performance of the designed ERL-FEL.[37] In the simulation, the normalized horizontal and vertical emittances are optimized for an electron bunch of 60 pC with a bunch length of about 1 ps at the entrance of the main linac by using the tracking code General Particle Tracer (GPT)[38] and a genetic algorithm.[17] GPT can calculate space charge effects, which are dominant in the beam dynamics of a low-energy electron beam.

The tracking code ELEGANT[39] simulates the electron beam from the main linac to the entrance of the FEL system. The bunch is accelerated off-crest up to 800 MeV by the main linac and then compressed down to 50 fs RMS or less with a momentum spread of about 0.1% in the 1st arc section. The R_{56} value of the 1st arc section is set to 0.31 m, and the DBA optics is

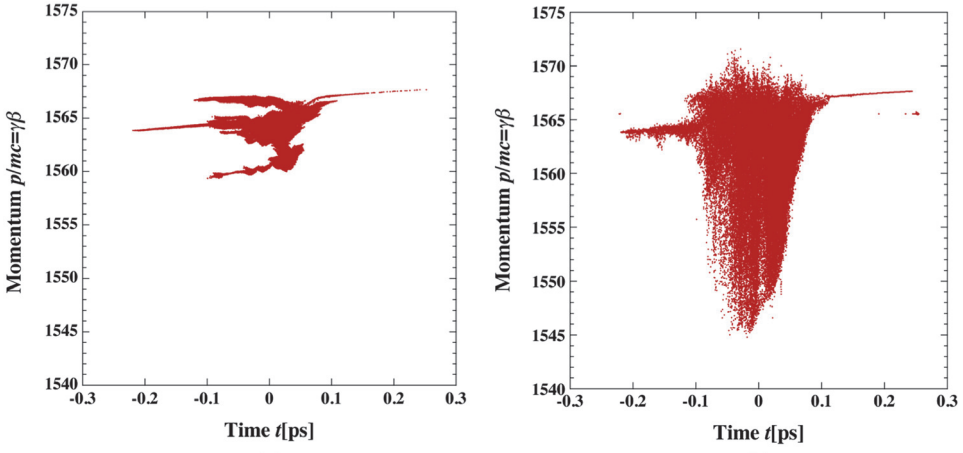

Figure 25.18 Time–momentum (t–p) distributions in the electron bunch at (a) the entrance and (b) the exit of the undulator system. The momentum spread is increased by the FEL lasing. (Adapted from Ref. 37.)

tracked by ELEGANT. The bunch is decompressed in the 2nd arc for which the R_{56} value is set to -0.25 m. The beam is then decelerated off-crest for energy recovery and sent to the dump line. In the S2E simulation, the beam is well transported, without serious beam loss, through the entire ERL-FEL light source with appropriate beam-pipe apertures, providing more than 10-kW power at less than 10 mA.

25.4 Design Concept of the Optics from the EUV-FEL to the EUV Scanner

An accelerator-based EUV-FEL will produce a high-power EUV light source, with more than 10 kW of output power. However, it is expected that the initial cost will be almost one order of magnitude higher than the current 250-W LPP EUV light source. Therefore, it is important to reduce the cost per scanner system. Figure 25.19 is a schematic view of the future LSI (large-scale integration) Fab based on an EUV-FEL light source as described by several authors.[41–43] In order to reduce the cost/scanner, the FEL light is delivered to 10 scanners by an arrangement of grazing-incidence curved mirrors. Of course, a redundant EUV-FEL must be prepared as shown in this figure reduce the down time of the light source.

In this section, a conceptional design of the optical system to deliver the FEL light to the multiple scanners is described. One of the issues is how to send the FEL light to multiple scanners without causing irradiation damage to the optical components. The most serious problem is expected to be an ablation effect at the high peak intensity of the EUV-FEL. As described in the

Chapter 26
UV Lamps for Lithography

Hisakazu Ieuji
Ushio, Inc., Tokyo, Japan

26.1 Introduction

Super-high-pressure mercury lamps are used as a light source not only for photolithography, but also for optical equipment, cinema projectors, and data projectors.[1]

The history of discharge lamps is long, dating back approximately 200 years. Discharge lamps were first researched and developed as light sources. They used two carbon rods in the atmosphere as electrodes to form an arc. In the 1900s, discharge lamps were developed in which metal vapor sealed in glass bulbs was used to form an arc. Because of the advantages of metals with high vapor pressure at low temperatures, mercury lamps were first developed by Cooper Hewitt in 1901.[2] Subsequently, sodium lamps were developed around 1920.[3] However, mercury lamps have a pale emission color, and sodium lamps have an orange emission color; both lamp types have poor color-rendering

(8) Base

The base is attached to both sides of the lamp to ensure electrical continuity and to adjust and set the lamp in the lamp house.

26.2.4 Characteristics

The characteristics of super-high-pressure mercury lamps can be broadly divided into four categories: optical, electrical, thermal, and lifetime characteristics. To understand the characteristics required for lamps used for lithography, the method of lamp usage inside the lithography equipment is described below. As an example, a simplified diagram of the most commonly used lens-type reduction optical system for semiconductor lithography equipment is shown in Fig. 26.4.

The light emitted by the lamp is focused by an elliptical mirror and passes through an integrator to enhance the uniformity of the irradiated surface and reaches the mask (reticle) surface through several lenses. The mask image is then projected onto the wafer surface using a reduced-projection lens.

The following are the light source requirements for such equipment:

1. A maximized amount of light incident on the elliptical mirror.
2. A narrow band of light wavelengths to reduce chromatic lens aberration.
3. A radiant body shape as close as possible to a point light source to increase the image resolution.

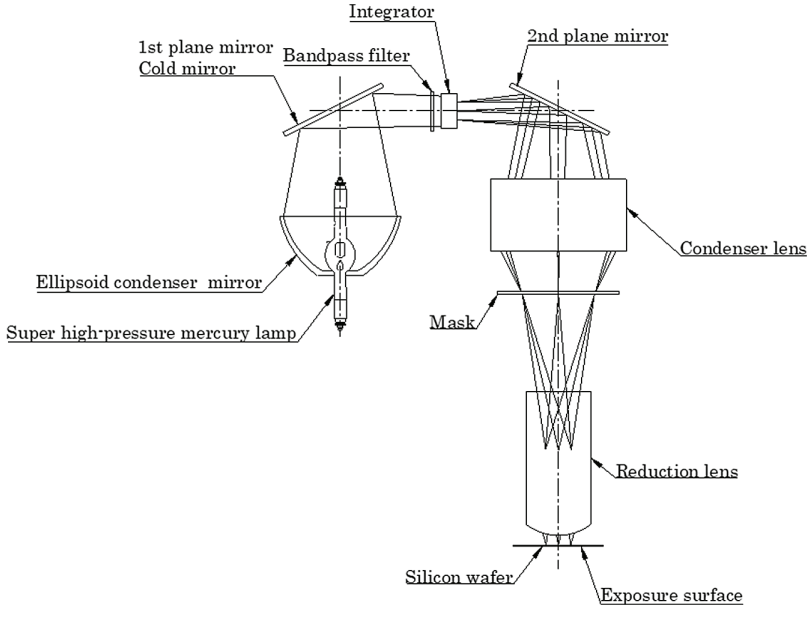

Figure 26.4 Simplified diagram of the lens-type reduction projection exposure system.

4. Low degradation of illumination intensity throughout operation for stable production.
5. Prevention of ignition failure or damage.

26.2.4.1 Optical properties

The three basic optical characteristics of a super-high-pressure mercury lamp are expressed in terms of the spectral distribution, radiant intensity distribution, and radiance distribution. Details of these characteristics and their representative data are described below followed by the optical characteristics and thermal properties.

(1) Spectral distribution

The spectral distribution is normally measured by the light emitted from a lamp. The distance to the lamp should be such that the heat generated by the lamp does not affect the distribution measurement. As mentioned above, the spectral distribution depends on the amount of mercury enclosed in the lamp. As the amount of mercury is increased in a lamp only under the same conditions, the continuous spectrum emission increases, and the emission spectrum line width increases. Figure 26.5 shows the spectral distribution of lamps with varying amounts of mercury. The emission line spectra around 365, 405, and 436 nm are called the i-line, h-line, and g-line, respectively. As the amount of mercury is reduced, the peak intensity of the emission line spectrum increases, while the emission line width decreases. For example, as shown in Fig. 26.2, the i-line is composed of four emission line spectra at

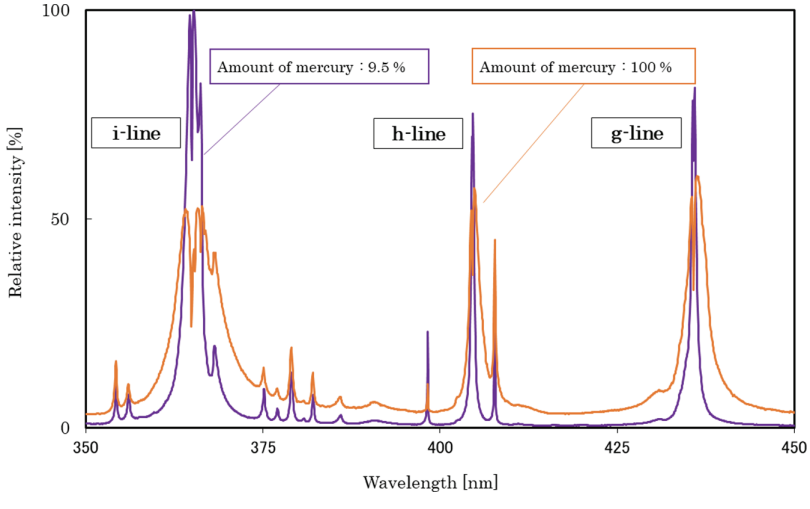

Figure 26.5 Spectral distributions of the same lamp design with different amounts of mercury. The orange line shows the case of a typical amount of mercury, and the purple line shows a reduced amount to 9.5% of the typical case.

Chapter 3

Atomic Xenon Data

John D. Gillaspy

[This appendix is reprinted from *EUV Sources for Lithography*, V. Bakshi, Editor, SPIE Press Vol. PM149 (2006).]

3.1 Introduction

The focus of this chapter is on fundamental *atomic* data; other sorts of fundamental data (related to the erosion of surfaces by plasma ions, for example) may be needed

Chapter 4

Atomic Tin Data

I. Yu. Tolstikhina, S. S. Churilov, A. N. Ryabtsev, and K. N. Koshelev

[This appendix is reprinted from *EUV Sources for Lithography*, V. Bakshi, Editor, SPIE Press Vol. PM149 (2006).]

4.1 Introduction

A spectrum of Sn in the region around 135 Å arises from transitions in Sn ions with the 4d electrons in the ground configuration. Because of the very complex structure of these transitions, the spectrum is largely unknown. Only four lines were identified in Sn XIV, where the ground configuration is $4p^6 4d$. We made calculations of the energy levels and transition probabilities in the Sn VI–XV spectra using the Flexible Atomic Code (FAC). Some results of similar calculations made with the aid of the Cowan code also can be found in Chapter 5. The spectrum of Sn excited in a low-inductance vacuum spark was recorded on a high-resolution grazing-incidence spectrograph in the region 100–200 Å and compared with the results of